Zebrafish models of human-duplicated gene *SRGAP2* reveal novel functions in microglia and visual system development

Authors:

José M. Uribe-Salazar[1], Gulhan Kaya[1], KaeChandra Weyenberg[1], Brittany Radke[1], Keiko Hino[2], Daniela C. Soto[1], Jia-Lin Shiu[2], Wenzhu Zhang[2], Cole Ingamells[1], Nicholas K. Haghani[1], Emily Xu[1], Joseph Rosas[2], Sergi Simó[2], Joel Miesfeld[3], Tom Glaser[2], Scott C. Baraban[4], Li-En Jao[2], Megan Y. Dennis[1†]

[1]Genome Center, MIND Institute, and Department of Biochemistry & Molecular Medicine, University of California, Davis, CA, USA
[2]Department of Cell Biology and Human Anatomy, University of California, Davis, CA, USA
[3]Department of Ophthalmology and Visual Sciences, Medical College of Wisconsin, WI, USA
[4]Department of Neurological Surgery and Weill Institute for Neurosciences, University of California, San Francisco, CA, USA

[†]Corresponding author:
Megan Y. Dennis, Ph.D.
University of California, Davis, School of Medicine
One Shields Avenue
Genome Center, 4303 GBSF
Davis, CA 95616
Email: mydennis@ucdavis.edu

Keywords: gene duplication, human evolution, zebrafish, *Danio rerio*, brain development, eye development, microglia

Abstract

Recent expansion of duplicated genes unique in the *Homo* lineage likely contributed to brain evolution and other human-specific traits. One hallmark example is the expansion of the human *SRGAP2* family, resulting in a human-specific paralog *SRGAP2C*. Introduction of *SRGAP2C* in mouse models is associated with altering cortical neuronal migration, axon guidance, synaptogenesis, and sensory-task performance. Truncated, human-specific SRGAP2C heterodimerizes with the full-length ancestral gene product SRGAP2A and antagonizes its functions. However, the significance of *SRGAP2* duplication beyond neocortex development has not been elucidated due to the embryonic lethality of complete *Srgap2* knockout in mice. Using zebrafish, we showed that *srgap2* knockout results in viable offspring that phenocopy "humanized" *SRGAP2C* larvae. Specifically, human SRGAP2C protein interacts with zebrafish Srgap2, demonstrating similar Srgap2 functional antagonism observed in mice. Shared traits between knockout and humanized zebrafish larvae include altered morphometric features (i.e., reduced body length and inter-eye distance) and differential expression of synapse-, axogenesis-, vision-related genes. Through single-cell transcriptome analysis, we further observed a skewed balance of excitatory and inhibitory neurons that likely contributes to increased susceptibility to seizures displayed by *Srgap2* mutant larvae, a phenotype resembling *SRGAP2* loss-of-function in a child with early infantile epileptic encephalopathy. Single-cell data also pointed to strong microglia expression of *srgap2* with mutants exhibiting altered membrane dynamics and likely delayed maturation of microglial cells. *srgap2*-expressing microglia cells were also detected in the developing eye together with altered expression of genes related to axogenesis and synaptogenesis in mutant retinal cells. Consistent with the perturbed gene expression in the retina, we found that *SRGAP2* mutant larvae exhibited increased sensitivity to broad and fine visual cues. Finally, comparing the transcriptomes of relevant cell types between human (+*SRGAP2C*) and non-human primates (–*SRGAP2C*) revealed significant overlaps of gene alterations with mutant cells in our zebrafish models; this suggests that *SRGAP2C* plays similar roles altering microglia and the visual system in modern humans. Together, our functional characterization of zebrafish Srgap2 and human SRGAP2C in zebrafish uncovered novel gene functions and highlights the strength of cross-species analysis in understanding the development of human-specific features.

Introduction

Genetic factors contributing to phenotypic differences between humans and non-human primates remain largely undiscovered [1,2]. However, gene expansion [3,4] has been suggested as an important driver of primate species divergence [5–13], as demonstrated through expression of human-specific paralogs in mammalian organismal and organoid models that recapitulate hallmark features of human brain development, including synaptogenesis, corticogenesis, and gyrification [14–20]. One of the most well-studied human duplicated genes is the Slit-Robo Rho GTPase-activating protein 2 (*SRGAP2*) [14,18,21–25]. *SRGAP2* paralogs have arisen over the last ~3.4 million years along human chromosome 1, resulting in a conserved ancestral full-length *SRGAP2* and three truncated forms of human-specific paralogs, *SRGAP2B*, *SRGAP2C*, and a likely nonfunctional *SRGAP2D* [23] (Figure 1A). Broadly, SRGAP proteins modulate cytoskeleton dynamics and membrane deformation when dimerized through their F-BAR domains by interacting with F-Actin, with potential implications for vital cellular processes such as motility, polarity, and morphogenesis [26]. The human ancestral *SRGAP2A* encodes a protein with F-BAR, RhoGAP, and SH3 domains. However, truncated *SRGAP2B* and *SRGAP2C* paralogs encode only the F-BAR domains [26], dimerizing with the F-BAR domain of SRGAP2A, leading to the degradation of the resulting heterodimer via the proteasome pathway [21,24]. As a result, expressing human-specific *SRGAP2C* in mouse models consistently phenocopies *Srgap2* knockdown/knockout, including increased rate of neuronal migration, neurite outgrowth, increased density of dendritic spines, and neoteny in the spine maturation process [21]. Further, *Srgap2* has important functions in synapse maturation and connectivity via interactions with Homer, Gephyrin, and Rac1, the known regulators of both excitatory and inhibitory synapse maturation [18,24]. In addition, conditional knockouts of *Srgap2*, knockdown of *Srgap2*, as well as introducing *SRGAP2C*, results in delayed neuronal maturation and increased densities of synapses in murine cortical pyramidal neurons [18,24]. Expressing *SRGAP2C* also leads to an increase in long-range synaptic connectivity in mouse cortical pyramidal neurons and enhanced cortical processing abilities in the whisker-based texture-discrimination tests [22]. Together, these studies support the contribution of *SRGAP2C* to the emergence of unique neuronal features and cognitive capacities in humans.

The embryonic lethality of complete *Srgap2* loss-of-function in mouse models [27] has limited global assessments of its functions in development. Here, we generated zebrafish *srgap2* "knockout" models resulting in viable offspring, providing us an opportunity to characterize *SRGAP2* developmental functions beyond the neocortex. We compared phenotypes with *SRGAP2C*-expressing "humanized" larvae by performing morphological, gene expression, cellular, molecular, and behavioral assays. We consistently observed concordant effects in *srgap2* knockout and *SRGAP2C*-humanized larvae across all assays, demonstrating that human-specific SRGAP2C antagonizes zebrafish Srgap2 functions. From these studies, we verified previous known functions of *SRGAP2* as an axon/synapse regulator. Leveraging our viable larvae, we found zebrafish mutants exhibited increased susceptibility to seizures, a screen not possible in the embryonic-lethal mice, strengthening findings of *SRGAP2* as an epilepsy gene [28]. We also propose a never-before-reported role of *SRGAP2* in the developing eye that impacts vision. Finally, we present evidence that *SRGAP2* is a conserved core gene in microglia function across vertebrates that alters membrane dynamics and delays maturation resulting in functions yet to be explored. In all, our zebrafish models support previous studies and expand on the possible roles that *SRGAP2C* play in the evolution of human features.

Results

Genomic and transcriptional conservation of *srgap2* zebrafish ortholog

The current zebrafish genome (GRCz11/danRer11) carries a single ortholog *srgap2* encoding F-BAR, RhoGAP, and SH3 domains. Human full-length SRGAP2 and zebrafish Srgap2 proteins share 73.8% amino acid identity, placing them phylogenetically closer than with other members of the SRGAP protein family (SRGAP1/SRGAP3 or Srgap1a/Srgap1b/Srgap3) (Figure 1A). The F-BAR domain of human SRGAP2—which forms homodimers with itself and heterodimers with paralogs SRGAP2B/C [21]—shares 87.9% amino acid identity with that of zebrafish Srgap2. Human SRGAP2C protein shows comparably high computationally-predicted [29] probabilities of inter-species interactions between zebrafish Srgap2 as with the mouse Srgap2 ortholog, previously shown to associate with the human paralogs [18,21,24] (Table S1). We experimentally confirmed the heterodimer interaction between zebrafish Srgap2 and human-specific SRGAP2C by performing co-immunoprecipitation in HEK293T cells (Figure 1B).

Published whole-embryo RNA sequencing (RNA-seq) [30] showed that expression of *srgap2* continues to increase after fertilization, plateaus after around 16 hours post fertilization (hpf), and persists thereafter, further confirmed with quantitative RT-PCR (Figure 1C). Initiation of *srgap2* expression coincides with critical neurogenesis periods that include the formation of post-mitotic neurons in the neural plate after gastrulation [31] occurring between 5.25 and 10 hpf [32]. Tissue-specific RNA-seq data from embryos (24 hpf) and adults (12 months old) [33] showed high *srgap2* expression in the embryonic head and adult brain with lower expression in viscera (e.g., heart, spleen, and kidney; Figure 1D). To validate these results, we performed whole-mount *in situ* hybridization and observed *srgap2* expression mainly in the developing central nervous system at 24 hpf and 3 days post fertilization (dpf) (Figure 1E). Thus, *srgap2* expression is spatiotemporally regulated during a critical period of early neurodevelopment in the zebrafish embryo and remains high in the adult brain [33]. These results suggest that zebrafish can serve as a suitable model to test *SRGAP2* paralog functions during neural development.

SRGAP2C humanized larvae phenocopy *srgap2* knockout models

We evaluated *SRGAP2* function during development using two different zebrafish knockout models (Figure 1F). First, we generated a stable *srgap2* knockout line carrying a 5-bp deletion in exon 4 using CRISPR mutagenesis (Table S2). While stable mutant lines are classically used for testing gene functions in zebrafish [34,35], we also characterized phenotypes in genetically-mosaic embryos carrying a mix of *srgap2* knockout alleles by injecting ribonucleoproteins containing SpCas9 coupled with four different guide RNAs (gRNAs) targeting early exons (termed "G_0 knockouts") [36–39]. Evaluation of 5 dpf mutant larvae revealed significantly decreased *srgap2* mRNA abundance in both knockout models (average relative reductions versus WT: Het= 23.8%, Hom= 59.7%, G_0 knockouts= 55.6%; Figure S1A). We observed no detectable off-target mutations in knockout larvae from either approach at the most probable sites predicted using CIRCLE-Seq and CRISPRScan (Table S3), suggesting that any observed phenotypes were due to the loss of Srgap2 function.

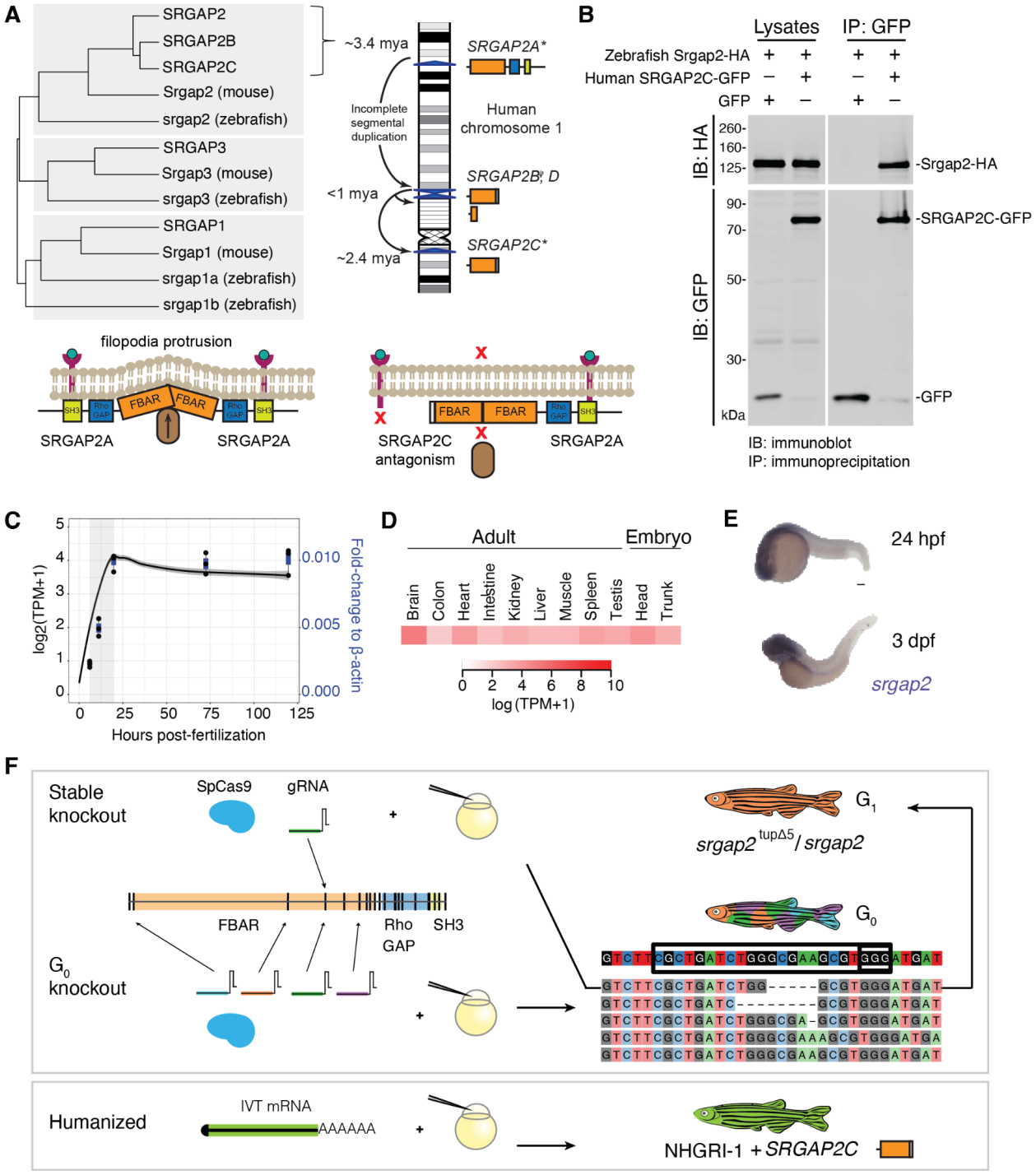

Figure 1. Functional analysis of *srgap2* in the developing zebrafish. (A) Phylogenetic tree of the human, mice, and zebrafish SRGAP proteins based on their whole-protein amino acid identity using the Unweighted Pair Group Method with Arithmetic Mean method. Schematic of *SRGAP2* gene family evolutionary history across human chromosome 1 [25]. Previous studies have shown that SRGAP2 functions after homodimerization in concert with F-actin (brown oval) to dictate cell membrane dynamics, among other functions, and can also heterodimerize with SRGAP2C producing no functional product. **(B)** Co-immunoprecipitation of human-specific SRGAP2C and zebrafish Srgap2 in HEK293T cells showed interaction between these proteins. **(C)** Temporal expression of *srgap2* in the developing embryo, plotted using public RNA-seq data [30] (black line represents the best fit line with the standard error in dark gray) and normalized quantitative RT-PCR data from whole-embryo RNA collected at 6, 10,

24, 72, and 120 hpf (blue boxes, each dot represents a biological replicate). The light-gray box represents a critical neurogenesis stage in zebrafish development between 6 and 24 hpf [31]. **(D)** *srgap2* expression in different embryonic (24 hpf) and adult (>12 months old) tissues from a published RNA-seq dataset [33]. **(E)** Spatial expression of *srgap2* at 24 hpf and 3 dpf via *in situ* hybridization. Scale bar 100 µm. **(F)** Knockout *srgap2* zebrafish were created using two approaches, one in a stable knockout line by injecting SpCas9 coupled with one gRNA targeting exon 4, and another following a pooled approach co-injecting SpCas9 coupled with four gRNAs targeting early exons. Humanized larvae were created by injecting *in vitro* transcribed *SRGAP2C* mRNA at the one-cell stage.

Initial assessment of batch siblings produced from crossing stable *srgap2* knockout heterozygous *srgap2*$^{tup\Delta5}$/*srgap2*$^{+}$ (Het) parents resulted in no difference in mortality at 5 dpf (survival curve test: χ^2= 2.96, df= 2, *p*-value= 0.228, n=148, WT= 19%, Het= 53%, Hom= 28%), which was recapitulated in G_0-knockouts versus scrambled gRNA controls (χ^2= 0.3, df= 1, *p*-value= 0.6, n G_0-knockouts= 347, n controls= 260). Morphological assessments [40,41] showed significant reductions in the length of the body axis (~4.4–7.6%) and distance between the eyes (~1.5–4.7%) of all *srgap2* knockout larvae (Het, Hom, and G_0) versus controls (Figure 2A). No significant effects on head-trunk angle, a feature typically used to estimate developmental timing in early zebrafish larvae [32], nor head area were observed, allowing us to rule out developmental delay (Figure S1B). Given the similarity of morphological features in both stable and mosaic knockout models, we primarily focused on phenotypes produced in G_0 knockout mutants moving forward.

We next generated a *SRGAP2C* humanized model by microinjecting *in vitro* transcribed mRNA into one-cell stage embryos (Figure 1F). This produced transient and ubiquitous presence of *SRGAP2C* transcripts in the developing zebrafish up to 72 hpf (Figure S1A), coinciding with peak endogenous *srgap2* expression (starting at 16 hpf; Figure 1C), with protein likely persisting for longer. *SRGAP2C*-humanized larvae developed normally with no increased mortality (survival curve test: χ^2= 0.8, df= 1, *p*-value= 0.4, *SRGAP2C*-injected= 422, eGFP-mRNA-injected controls= 308). They also exhibited significant changes in overall body length and distance between the eyes (~5.7% reduction in body length and ~4.2% reduction in distance between the eyes Figure 2A), similar to the phenotypes observed in the knockout models. Thus, expressing human SRGAP2C antagonized endogenous zebrafish Srgap2 function in developing zebrafish larvae, similar to what has been observed in the mouse models where human SRGAP2C attenuated mouse Srgap2 functions [14,18,21,24].

Transcriptomes reveal developmental impacts upon perturbation of Srgap2 function

Given that knocking out *srgap2* and expressing human *SRGAP2C* generated similar developmental phenotypes (Figure 2A), we reasoned that a common set of molecular processes were perturbed under these two experimental conditions. Comparing expression profiles of dissected heads from G_0 knockouts and *SRGAP2C*-injected embryos/larvae across early developmental stages, we observed high correlation of expression changes relative to their respective controls (Figures 2B and C, Note S1) and significant enrichment of shared differentially expressed genes (DEGs) between the models (e.g., 467 shared genes at 5 dpf, Fisher's exact test odds ratio= 378.3, *p*-value < $2.2\text{x}10^{-16}$, Table S4).

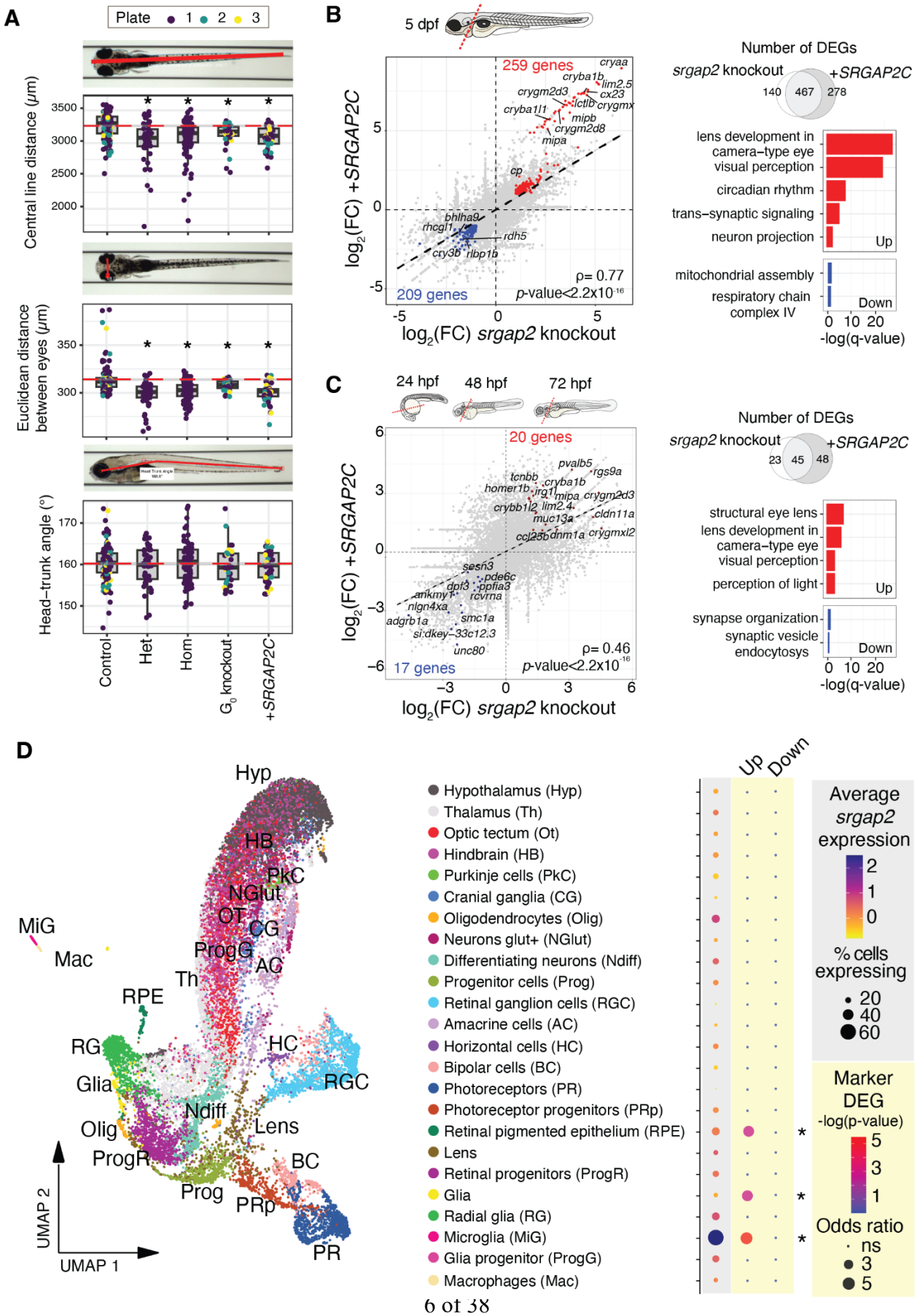

Figure 2. Developmental and cellular phenotypes of diverse zebrafish models of *SRGAP2*. (**A)** Measurements of central line distance (ANOVA: $F_{(4, 321)}$= 12.84, genotype effects *p*-value= $1.04x10^{-9}$, FDR-adjusted *p*-values Het= $4.40x10^{-7}$, Hom= $6.29x10^{-7}$, Pooled= 0.015, *SRGAP2C*= $1.36x10^{-4}$), euclidean distance between the eyes (ANOVA: $F_{(4,321)}$= 23.49, genotype effects *p*-value= $4.72x10^{-17}$, Dunnett's test FDR-adjusted *p*-values: Het= $6.77x10^{-11}$, Hom= $4.69x10^{-10}$, Pooled= 0.05, *SRGAP2C*= $2.19x10^{-9}$), and head angle (ANOVA: $F_{(4,315)}$= 0.49, genotype effects *p*-value= 0.746) in 5 dpf larvae from stable *srgap2* knockout (Het n= 43, Hom n= 86), G_0 knockouts (n= 34), *SRGAP2C*-injected (n= 44), and control larvae (n= 124). Dots represent an imaged larva with the color indicating the imaging plate (a co-variable included in the statistical analyses). The red dotted line corresponds to the mean value for the control group. Representative images of each measurement are included on the top of each plot. (**B)** Correlation of the fold change (FC) between *srgap2* G_0-knockouts and *SRGAP2C*-injected larvae at 5 dpf, with common DEGs highlighted (red= upregulated (FC > 2), blue= downregulated (FC < -2)). Top representative GO terms enriched in common DEGs between *srgap2* G_0-knockouts and *SRGAP2C*-injected larvae (complete results in Table S5). Color of the bar represents the direction of the genes (red= commonly upregulated, blue= commonly downregulated). (**C)** Correlation of the FC between *srgap2* G_0-knockouts and *SRGAP2C*-injected larvae across development using data from 24, 48, and 72 hpf larvae, with common DEGs highlighted, complete results can be found in Tables S7, S8. (**D)** Clustering of the 28,687 profiled cells colored as 24 cell types based on the expression of gene markers. Expression of *srgap2* across cell types (left side, shaded in gray), with the size of the circle representing the percentage of cells in that cluster expressing *srgap2* and the color of the circle the average scaled expression in the cluster. Enrichment test for the overlap between marker genes for each cell type and the differentially expressed genes at 3 dpf from bulk RNA-seq data (right side), with the size of the circle representing the odds ratio for the enrichment and the color of the circle the -log(BH-adjusted *p*-value) of the Fisher's exact test. Asterisks indicate an FDR-adjusted *p*-value < 0.05.

Specifically, we found that shared upregulated genes were overrepresented in gene ontology (GO) terms across all developmental time points related to lens and visual system development (Tables S4-S8). For older larvae (5 dpf), unique upregulated genes were largely related to neurodevelopment (mainly neuronal projections and synapse organization) and circadian rhythm, while downregulated genes were significantly overrepresented in mitochondrial cytochrome c oxidase assembly (Figures 2A). Mitochondrial dysfunction is associated with reduced height [42], consistent with the reduced body axis observed in our larvae. Alternatively, younger mutant embryos (1, 2, 3 dpf) exhibited downregulation of genes related to synapse organization suggesting delayed synaptic maturation during these earlier developmental time points. In particular, *ppfia3*, a regulator of presynapse assembly [43], was found significantly upregulated in 5 dpf larvae while downregulated in embryos (≤ 3 dpf). These results align with results observed in *Srgap2* knockdown or *SRGAP2C*-expressing mouse embryos that exhibit neoteny of synaptogenesis [18]. Together, through identifying the common pathways affected in the *srgap2* knockout and *SRGAP2C*-humanized zebrafish models, Srgap2 seems to play a critical role in the development of the visual systems and neurodevelopment.

To narrow in on the cell types driving expression changes, we performed single-cell transcriptomic profilings (SPLiT-seq [44]) of 28,687 single cells isolated from 3 dpf zebrafish larval brains (Table S9). Using expression patterns of marker genes [45,46], we classified 24 cell types and found broad *srgap2* expression across neuron-containing clusters, with highest expression in microglia (Figure 2D, Tables S10 and S11). Overlaying these cell markers with DEGs observed in bulk RNA-seq analysis, we observed significant enrichment of upregulated DEGs for retinal pigmented epithelium (RPE), glia, and microglia cells (Figure 2D, Table S12).

Synaptic alterations in *SRGAP2* zebrafish models

Based on its broad neural expression pattern, we performed pseudo-bulk analyses across 11,450 neuronal cells revealing overrepresentation in GO terms of upregulated genes (n=14) related to neuron projection guidance between *SRGAP2* models. In particular, we observed significant upregulation of *ephb2*, implicated in promoting/directing axon guidance across the brain midline [47,48]. Downregulated genes (n=21) were enriched for synaptic signaling functions, concordant with bulk RNA-seq results (Figure 3A, Tables S13 and S14). Narrowing in on neuronal subtypes driving these differences, markers for forebrain, midbrain, and differentiating neurons were enriched in upregulated genes; while hindbrain and the broad neuron category were enriched for downregulated genes (Figure 3A, Table S15, BH-adjusted Fisher's exact tests p-values < 0.05).

Given findings of altered synaptic signaling/organization and the role of *SRGAP2* paralogs in regulating synapses in mice [18] (Figure 2B), we narrowed in on excitatory (Exc; *slc17a6b*/*vglut2*) and inhibitory (Inh; *gad1b*) neuronal subtypes in our scRNA-seq data [45,46]. Comparing relative abundances across models showed that both *srgap2* knockouts and *SRGAP2C*-injected larvae exhibited a ~20% increase in the Exc:Inh ratios (Figure 3B). Quantifying co-labeled GABAergic (Tg[*dlx6a*:GFP] [49]) and glutamatergic (Tg[*vglut2a:*DsRed] [50]) neurons validated these results, with a ~29% increase in the Exc:Inh ratio relative to uninjected wild-type and control-injected larvae (Figure 3C). Control results matched previous studies using the same transgenic lines of the same age [51] (wild-type controls Exc:Inh ratio= 0.98±0.04).

A skew in higher excitatory versus inhibitory neuronal balance is associated with seizures, as has been reported in several zebrafish epilepsy models [52]. We first assessed chemically-induced seizure-like behaviors [53] by counting high-speed movement events (HSE, >28 mm/s) in 4 dpf larvae exposed to either a low concentration of pentylenetetrazole (PTZ, 2.5 mM) or to E3 media (control). While HSE were rare in non-PTZ-treated larvae with no difference in frequency between groups (average HSE/min= 0.006±0.02; Figure 3D), the addition of PTZ significantly increased the frequency of HSE on average by 0.31±0.08 min^{-1} in *srgap2* knockouts and *SRGAP2C*-humanized larvae compared to controls. Next, we detected spontaneous electrographic seizures by recording local field potentials (LFP) [53]. *SRGAP2C* larvae experienced ictal-like Type II electrical events classifying them as epileptic (n= 21, LFP score= 1.45, Figure 3E), while control (n= 22) and *srgap2* G_0-knockouts (n= 30) did not exhibit any events. Strikingly, *SRGAP2C* larvae showed LFP scores in the range observed in zebrafish models of well-established epilepsy-associated genes (e.g., *SCN1A*, *STXBP1*) [53], highlighting a potential true effect in their susceptibility to experience unprovoked seizures. Overall, our results point to a role of SRGAP2 and its human-specific paralog *SRGAP2C* in maintaining neuronal E:I balance and potentially contributing to seizure susceptibility.

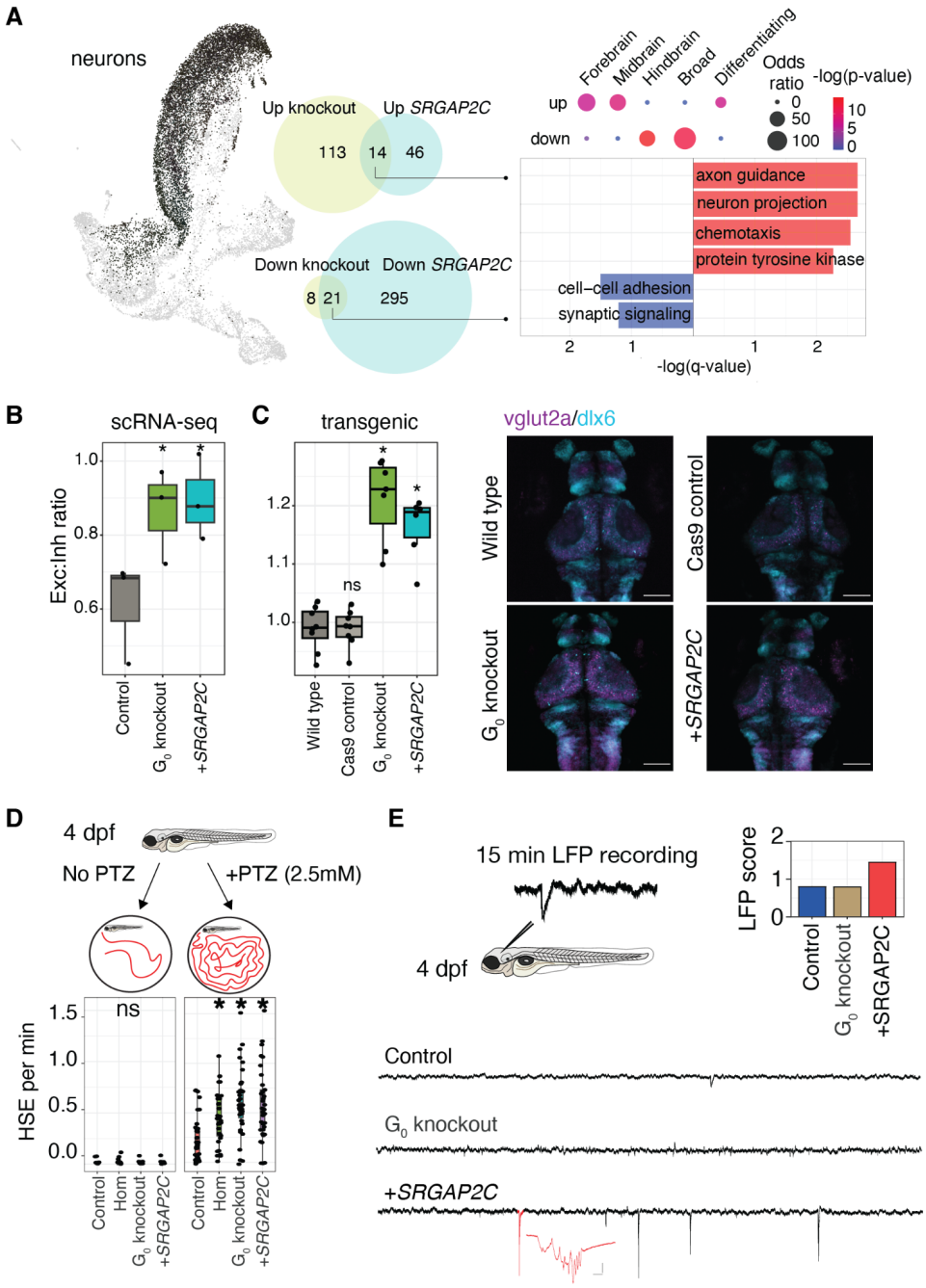

Figure 3. Neuronal alterations in *SRGAP2* mutants. **(A)** Neuronal clusters (hypothalamus, thalamus, optic tectum, hindbrain, purkinje cells, and neurons rich in glutamate receptors) selected to perform a differential gene expression test was performed to DEGs in the *SRGAP2* mutants compared to the control group. Barplot represents the top GO terms overrepresented in the 14 commonly upregulated genes (complete results in Table S14). **(B)** Ratio of cells classified as excitatory (*vglut2*$^{+}$) to inhibitory (*gad1b*$^{+}$) between the *srgap2* G_0-knockouts, *SRGAP2C*-injected, and controls (*srgap2* G_0 knockouts: 0.78±0.15, *p*-value= 0.031; *SRGAP2C*-injected: 0.82±0.09, *p*-value= 0.017, controls= 0.57±0.13; t-tests versus controls). **(C)** Ratio of excitatory (*vglut2*:DsRed+) to inhibitory (*dlx6*:GFP) cell area quantified from images of 3 dpf *srgap2* G_0-knockout, *SRGAP2C*-injected, SpCas9 control injected, and uninjected wild type larvae (G_0 knockout: Exc:Inh ratio=1.21±0.07, *p*-value=3.0x10^{-4}, *SRGAP2C*: Exc:Inh ratio= 1.16±0.05, *p*-value= 7.0x10^{-4}, SpCas9-injected controls Exc:Inh ratio= 0.98±0.03, p-value= 0.959; Mann-Whitney U-tests *p*-values vs wild-type controls). Images include representative samples per group, scale bars 100 µm. **(D)** High-speed events (HSE, >28 mm/s) identified in 15 min recordings of 4 dpf larvae (*srgap2* knockouts

(stable Hom_{parent} and G_0), *SRGAP2C*-injected, and SpCas9-injected controls, n= 36 larvae per group) with and without PTZ. Frequency of HSE per min were compared to controls (0 mM PTZ: ANOVA *p*-value for genotypic effect= 0.415, average HSE/min= 0.006±0.02, no significant differences between groups; 2.5 mM PTZ: ANOVA genotype effect *p*-value= 1.1x10-6, Hom_{parent}= 0.010, G_0-knockouts= $2.2x10^{-6}$, *SRGAP2C*-injected= $3.90x10^{-5}$). **(E)** Local field potential (LFP) recordings in the optic tectum of 4 dpf larvae (G_0-knockouts, *SRGAP2C*-injected, and SpCas9-injected controls, n=21-30 per group) were obtained and scored by two independent researchers. Representative traces per group are shown. Asterisks in graphs represent a *p*-value below 0.05 for the comparison against the control group. ns= not significant.

SRGAP2 is a conserved microglial gene impacting ramifications

Moving beyond neurons, we observed the highest expression of *srgap2* in microglia (Figure 3D), concordant with a previous study implicating *SRGAP2* as a "core" microglia gene with high conservation across human, macaque, marmoset, sheep, rat, mouse, hamster, and zebrafish [54]. When comparing transcriptomes of microglia cells from both *srgap2* knockout and *SRGAP2C*-expressing zebrafish models versus controls, we found that upregulated genes (n=38) were enriched for GO terms in cell migration and downregulated genes (n=65) were overrepresented in actin-mediated filopodia processes (Figure 4A, Tables S16 & S17). These results aligned with the ability of SRGAP2 to induce cell projections in concert with F-actin [55,56]. Since microglia also develop complex cell ramifications, we hypothesized that their cell-membrane dynamics were also modulated by Srgap2 activity (e.g., via SRGAP2C antagonization).

To test this, we characterized microglia in our *srgap2* G_0 knockouts and humanized *SRGAP2C* models. While there was no difference in microglia abundance [57] (Figure S2), we observed significantly reduced ramifications (quantified as increased sphericity) compared to controls at both 3 and 7 dpf using a transgenic line labeling macrophages (Tg[*mpeg1.1*:GFP], Figure 4B) [58]. By these developmental time points, macrophages are generally accepted to be microglia (or their precursors) when localized in the brain/retina of zebrafish [59]. The microglia in control larvae continued to acquire more ramified morphologies from 3 to 7 dpf as they matured (t-test of 3 vs 7 dpf: t= 2.97, *p*-value= 0.0055, Figure 4B), concordant with previous reports [60]. Alternatively, microglia in both *SRGAP2* models retained similar sphericity at both timepoints (t-tests per mutant genotype *p*-values > 0.05), suggesting arrested maturation. While our results point to delayed microglia development in our *SRGAP2* mutant larvae, we cannot rule out increased microglia activation, which also involves morphological changes from a ramified "resting" state to more ameboid-like active shapes [61,62]. This was supported, in part, by upregulation of known microglial activation markers (*hsp90aa1.1* and *zfp36l2*) observed in our *SRGAP2* mutants at 5 dpf [63] from bulk RNA-seq results.

To examine if SRGAP2/C might contribute to human-specific microglia membrane dynamics, we re-analyzed published single-cell transcriptomes of 610,596 prefrontal cortex cells from human, chimpanzee, macaque, and marmoset [64]. In line with its conserved "core" characterization [54], *SRGAP2* exhibited highest expression in the microglia clusters in all primates (Figure 4C), including human- and hominidae-specific microglia subclusters (Figure 4D, Note S2, Table S18). *SRGAP2C* expression also was high in all human microglia subtypes, albeit slightly lower compared to *SRGAP2*. Taking an analogous pseudo-bulk approach to our zebrafish analysis, we compared gene expression of human (+*SRGAP2C*) versus chimpanzee, macaque, or marmoset (-*SRGAP2C* "controls") microglia. Human DEGs were consistent with reduced microglia ramifications, including downregulation of genes associated with cell projection and the plasma membrane (Table S19). We also observed upregulation of genes implicated in

extracellular matrix and inflammatory response, both features of migrating microglia in an ameboid state. Examining shared DEGs showed a significant overlap between human/primate and zebrafish *SRGAP2* mutants (Fisher's test odds ratio= 2.77, *p*-value= 0.0046; 10 overlapping genes= *BAIAP2L1, ZNF135, BOC, DCHS1, FOXP2, GGT1, ITGB7, PHLDB2, SGK1, ST6GAL2*). These results highlight that the alterations of microglial cell shape observed in our zebrafish *SRGAP2C* "humanized" models recapitulate human-specific biological processes that occur in microglial cells.

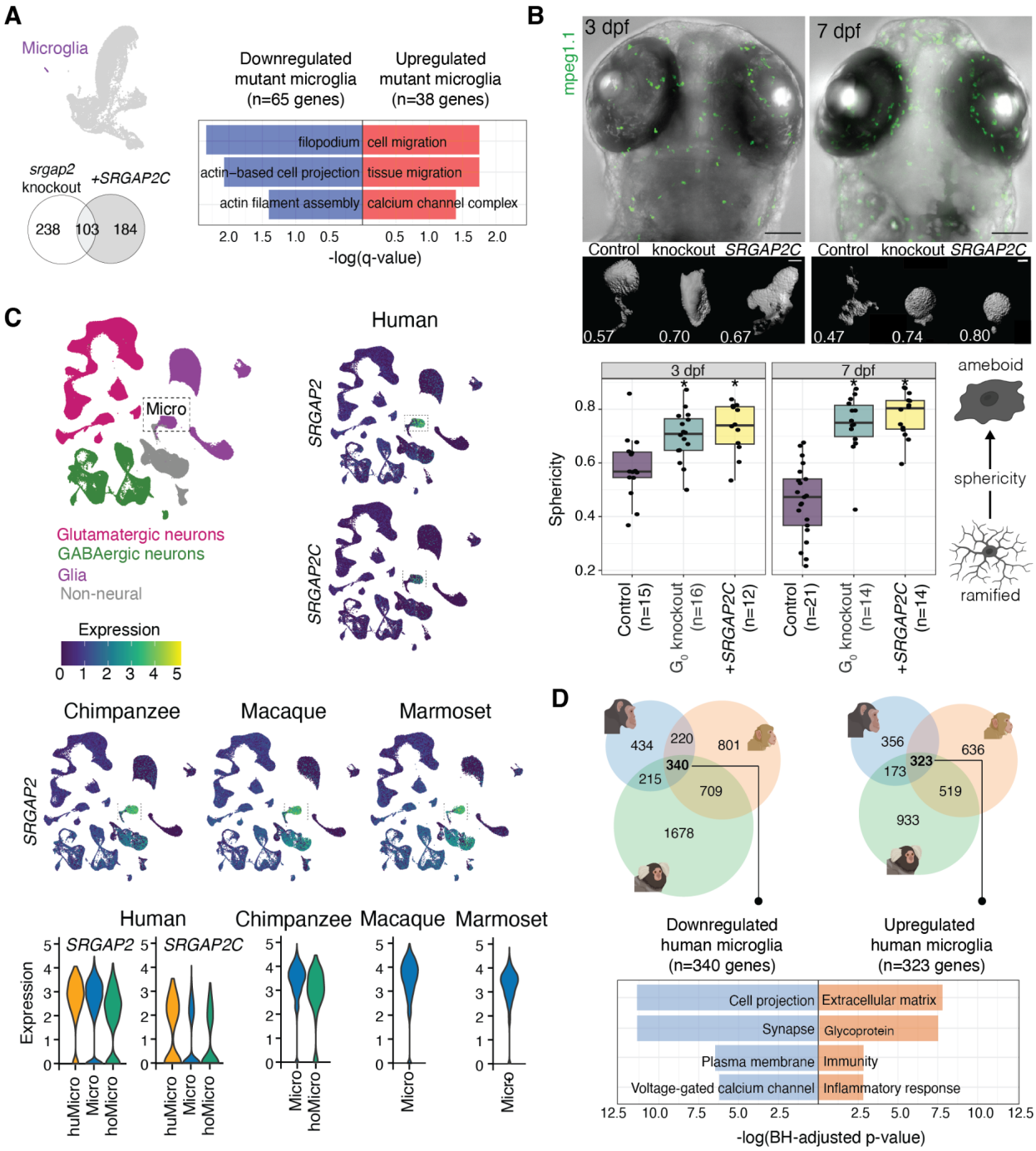

Figure 4. Cross-species conservation of *SRGAP2* as a microglial gene. **(A)** Top GO terms with significant overrepresentation in genes upregulated (red) or downregulated (blue) in microglial cells from *SRGAP2* mutants from Figure 2D. **(B)** Sphericity values for individual microglial cells (mpeg1.1^{+}) at 3 and 7 dpf in *srgap2* knockouts, *SRGAP2C*-injected, and scrambled gRNA-injected controls. Each dot represents a single microglial cell (average of 4-5 cells per larvae from 3-4 larvae per genotype per timepoint were obtained). Representative images for the median sphericity value of larvae at 3 and 7 dpf for each genotype are included below the graph (scale bars: top images= 100µm, bottom images= 5 µm) . Asterisks denote a Tukey *post*-hoc p-value < 0.05. 3dpf: *srgap2* G_0 knockouts: 0.70±0.09, *p*-value= 0.0085; *SRGAP2C*-injected: 0.73±0.09, *p*-value= 0.0021, controls: 0.58±0.12; 7dpf: *srgap2* G_0 knockouts: 0.74±0.11, *p*-value < $2.2x10^{-16}$; *SRGAP2C*-injected: 0.78±0.08, *p*-value < $2.2x10^{-16}$, controls: 0.46±0.13. **(C)** Evaluation of 610,596 prefrontal cortex cells from human, chimpanzee, macaque, and marmoset (human: 171,997, chimpanzee: 158,099, macaque: 131,032, marmoset: 149,468) showing the levels of *SRGAP2* and *SRGAP2C* expression across species, highlighting the microglial cluster with a dotted square. Micro: microglia. Expression of *SRGAP2* and *SRGAP2C* in microglial subtypes across species with subtypes ordered from highest expression left to right. huMicro: human-specific microglia, hoMicro: Hominidae-specific microglia. **(D)** Microglial cells from human, chimpanzee, macaque, and marmoset (human: 8,819 cells, chimpanzee: 6,000 cells, macaque: 9,000 cells, marmoset: 7,099 cells) from the prefrontal cortex and middle temporal gyrus were used to identify common DEGs between human and non-human primates, finding 340 common upregulated and 323 common downregulated genes. Top GO terms with significant overrepresentation in common DEGs are included.

Visual system alterations in *SRGAP2* zebrafish models

The most striking molecular changes in *SRGAP2* mutant zebrafish were upregulation of genes related to lens development and visual perception (Figure 2B & C). Morphologically, eyes of *srgap2* knockout and *SRGAP2C*-humanized zebrafish developed normally with the formation of all major cell types by 5 dpf (Figure S3). Performing RNA *in situ* hybridization (ISH) to examine *srgap2* function in more detail, we found predominant expression in the optic nerve (ON), RPE, and along the retinal ganglion cell layer (GCL) at 3 dpf (Figure 5A). While scRNA-seq data showed strong expression of *srgap2* and enrichment of differential marker genes in RPE cells, we found little to no *srgap2* expression in retinal ganglion cells (RGCs) comprising the GCL (Figure 2D). Instead, *srgap2* ISH likely marks microglia that have migrated into the retina, with strongest expression evident at the interface between the lens and the neural retina.

To understand biological impacts within the retina, we identified differentially expressed genes across RGCs and RPE cells in *SRGAP2* models versus controls. RGCs were enriched for upregulated genes related to stem-cell differentiation, neuron-projection extension, and amoeboid-type cell migration (Figure 5B, Tables S20 & S21). Upregulated genes in RPE were also associated with cell-cell adhesion as well as negative regulation of the smoothened pathway, which mediates response to Hedgehog signaling [65]. Genes downregulated both in RGCs and the RPE were overrepresented in extracellular structures (e.g., matrix metalloproteinases, laminin, and collagen gene families). Connecting our findings to the human retina (organoids [66,67] and post mortem [68,69]), transcriptomic data from human (+*SRGAP2C*) versus rhesus macaque (-*SRGAP2C* "controls") also show upregulation of similar pathways related to axon development and neuron projections. Again, we observed a significant overlap in common DEGs between cells from human retina and *SRGAP2* zebrafish mutant RGC/RPE (69 overlapping genes, Fisher's test odds ratio= 6.23, *p*-value< $2.2x10^{-16}$; Tables S22-S25 and Note S3). Together, these results point to unexplored human-specific eye development features facilitated by *SRGAP2C*—related to membrane dynamics impacting axogenesis—impacting retinal connectivity that is fundamental for visual information processing [70].

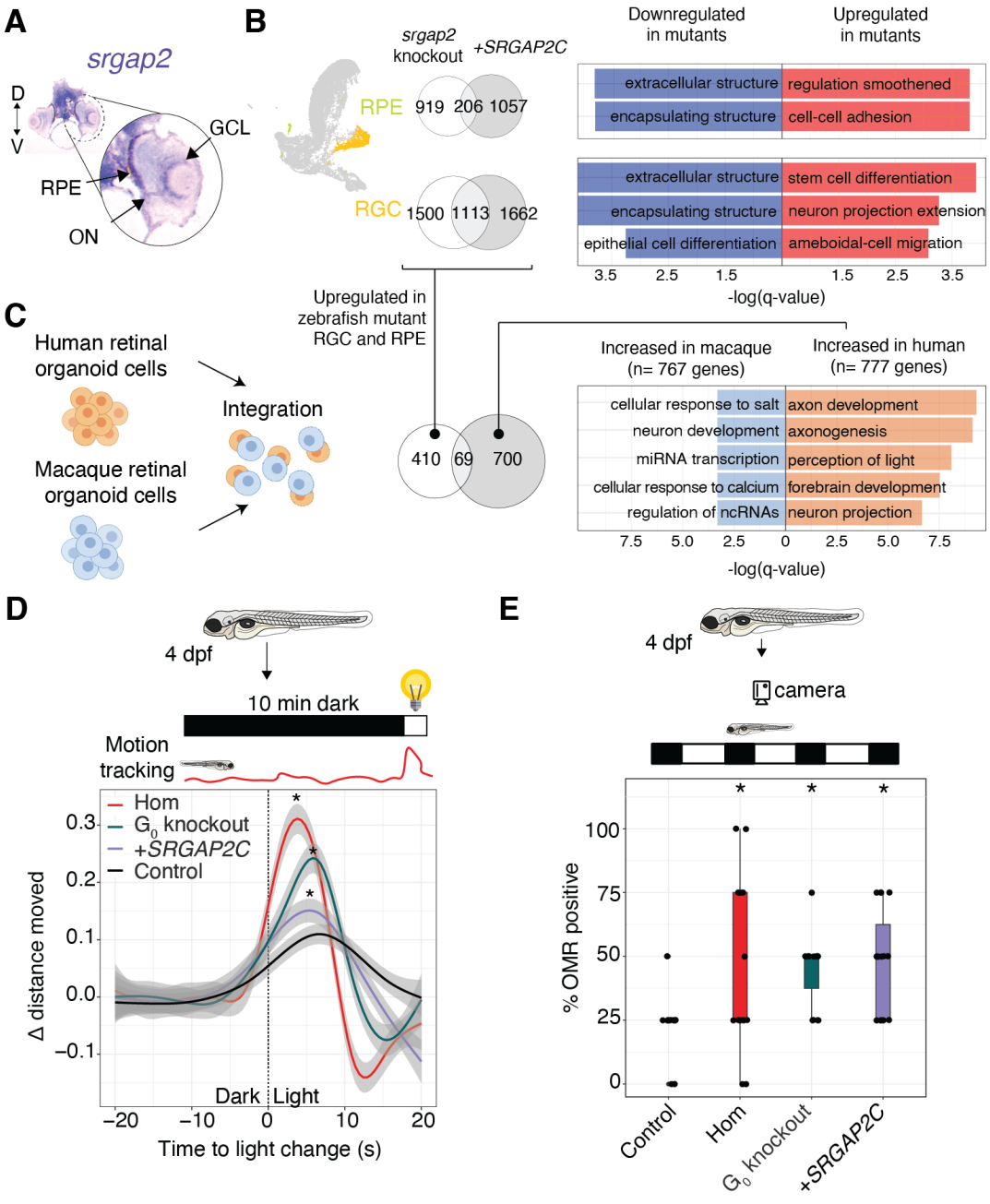

Figure 5. *SRGAP2* impacts the retina. **(A)** Section of a 3 dpf NHGRI-1 larva staining *srgap2* expression via *in situ* hybridization, labeling predominantly the optic nerve (ON), retinal pigmented epithelium (RPE), and the ganglion cell layer (GCL). D: dorsal, V: ventral. **(B)** Retinal ganglion cells (RGCs) were selected and a differential gene expression performed between *SRGAP2*-mutants (*srgap2* knockouts and *SRGAP2C*-injected) versus controls, identifying 60 upregulated genes and 84 downregulated genes, with their top overrepresented GO terms included in barplots. **(C)** Human and macaque cells from retinal organoids (43,857 human and 19,894 macaque) were integrated to identify genes with increased expression in either species, with their top overrepresented GO terms included in barplots (complete results in Tables S22 and S23). **(D)** Motion response to changes in light were assessed in 4 dpf *srgap2* knockouts (Hom_{parent} and G_0-knockouts), *SRGAP2C*-injected, and SpCas9-scrambled gRNA-coupled control larvae using a 10 min acclimation period followed by an abrupt light change. Plot includes trend lines for change in distance moved observed in each evaluated group (n= 24 per group, standard error for each line included as a shaded gray), which were different between all groups compared to controls (Kolmogorov-smirnov tests *p*-values: Hom_{parent}= $9.16x10^{-11}$, G_0-knockouts= $5.93x10^{-8}$, *SRGAP2C*-injected= $1.11x10^{-12}$). **(E)** Optomotor responses were

evaluated in 4 dpf larvae using an optimized protocol[71] that quantifies the percentage of larvae relative to moving stripes. Boxplot includes the percentage of OMR-positive larvae (aligned to the visual stimulus) in *srgap2* knockouts (Hom_{parent} and G_0-knockouts) and *SRGAP2C*-injected, which was higher compared to controls (Dunn's Benjamini-Hochberg adjusted *p*-values: Hom_{parent}= 0.0113, G_0-knockouts= 0.0040, *SRGAP2C*-injected= 0.0040). Asterisks denote a *p*-value below 0.05.

To assess if the observed molecular differences alter vision in our *SRGAP2* models, we leveraged natural zebrafish larval behavior that react to abrupt changes in light intensity with increased swimming activity [72,73]. Using motion tracking, we observed a significant increase in response to light stimulus in *SRGAP2* mutants (knockouts and *SRGAP2C*-injected) compared to controls (Figure 5D) at 4 dpf suggesting higher sensitivity to light changes. Considering our models exhibited increased susceptibility to seizures that could evoke similar responses, we also characterized more refined visual cues. The optomotor response (OMR) measures the instinctive behavior of free-swimming zebrafish larvae to align their body axis in the same direction as contrasting visual stimuli, such as moving stripes, which helps freshwater fish swim upstream [71,74,75]. We found that a larger percentage of 4 dpf *srgap2* knockouts (Hom_{parent} and G_0) and *SRGAP2C*-humanized showed OMR-positive positioning compared to the control group (n per group= 15, Figure 5E). Together, these results suggest that alteration of Srgap2 activity—either through genetic knockouts or human *SRGAP2C* expression—impacts the function of retinal microglia and possibly contributes to altered neuronal connectivity in the developing eye, leading to more sensitive neuronal responses to visual cues.

Discussion

SRGAP2, encoding a Slit-Robo Rho GTPase-activating protein, is a well-studied human-specific duplicated gene with a wealth of gain- and loss-of-function studies in diverse cell culture and mouse models. Its functions include regulating neuronal migration, synaptogenesis, and long-range connectivity in the central nervous system [14,18,22,24]. However, because of the embryonic lethality of the *Srgap2* knockout in mouse models, its functions beyond the neocortex are still largely left unexplored. Here, we present new functional analyses of *SRGAP2* in zebrafish, with viable knockout mutants that allow detailed screening of developmental phenotypes at an organismal level. For this purpose, we evaluated a diverse panel of zebrafish models in which the *srgap2* gene was disrupted or the truncated human paralog *SRGAP2C*, which heterodimerizes and antagonizes Srgap2 action (Figure 1B), was introduced. We observed an overall concordance in developmental phenotypes between *srgap2* knockouts and *SRGAP2C*-injected zebrafish larvae, similar to previous mouse studies where temporal expression of truncated *SRGAP2C* mirrored *Srgap2*-knockdown/knockout alleles [14,18,24]. For example, morphologically both *SRGAP2* model types (knockouts and "humanized" with *SRGAP2C*) consistently excited shorter body length, a phenotype not reported previously. This was perhaps driven by altered mitochondrial functions evident in our bulk RNA-seq analysis (Figure 2B) or perturbation to migration-dependent processes, such as muscle guidance and body patterning that are influenced by the Slit-Robo pathway [76,77].

Our bulk transcriptomic analyses of mutant zebrafish—ranging from 24 hpf embryos to 5 dpf larvae—also revealed alterations to known molecular functions, including increased axogenesis in *SRGAP2* mutants (knockouts and *SRGAP2C*-humanized) consistent with the gene's well-characterized role in axonal guidance via the Slit-Robo pathway [14]. We also observed downregulation of genes related to

synaptogenesis in early developmental embryos (24 hpf–3 dpf), concordant with neoteny of synaptogenesis in *SRGAP2* mouse models reminiscent of human brain development [18,24]. Leveraging single-cell transcriptomes allowed us to further narrow in on cellular mechanisms driving molecular signatures (Figure 2D). For example, focusing specifically on neurons in 3 dpf zebrafish, we observed upregulated axon-guidance genes most prominently in the forebrain, comprising the telencephalon and orthologous to the mammalian neocortex [78,79], and the midbrain region (Figure 3A) composed of optic tectum, the visual processing center in the zebrafish brain [80]. Downregulated synaptogenesis genes were found broadly across neurons and in the hindbrain. Based on these observations and the robust literature implicating *SRGAP2* in synaptogenesis [18,21,22,24], we cataloged neurons expressing Exc (glutamate) or Inh (GABA) neurotransmitters revealing increased Exc:Inh ratio in *SRGAP2* mutants.

Connecting the Exc:Inh imbalance with mechanism underlying epilepsy [52,81,82], we found an increased susceptibility to chemically-induced seizures (Figure 3C). *SRGAP2C*-expressing larvae also presented spontaneous, unprovoked, electrographic seizures not observed in our G_0 knockout mutant. Differences in phenotypic severity between the knockout and humanized models might be explained by genetic compensation as a result of nonsense-mediated decay in our knockout mutant [83]. Transcriptome data of *SRGAP2* mutant neurons provided additional clues to possible mechanisms underlying our observed phenotypes; for example, we observed significantly reduced expression of the *GRIN2A* ortholog (*grin2ab*, Table S13), encoding glutamate [NMDA] receptor subunit epsilon-1, with loss-of-function variants implicated in epileptic aphasia in humans [84]. These results are largely consistent with a clinical report of early infantile epileptic encephalopathy in a human child carrying a reciprocal translocation disrupting *SRGAP2* [28], providing evidence that mutations of this gene may contribute to epilepsy. We note that the embryonic lethality of *Srgap2* knockout mice has impeded similar evaluations in mammalian models to date.

Hallmark studies have shown that *Srgap2* loss-of-function or *SRGAP2C* expression leads to reduced filopodia in COS7 cells and fewer branching processes in mouse cortical neurons [14], impacting cell migration *in vivo* [21]. Our transcriptomes point to similar *SRGAP2* functions also in zebrafish microglia, with loss of Srgap2 function (through *srgap2* knockout or expressing *SRGAP2C)* associated with reduced expression of filopodia and actin-based cell projections-related genes and increased expression of cell migration genes. These molecular signatures were verified *in vivo*, with mutant zebrafish microglia exhibiting reduced ramifications versus controls. They also maintained an ameboid-like spherical shape through development time (3 to 7 dpf; Figure 4B) instead of the expected increased ramifications observed in a typically-developing zebrafish larva [60]. This ameboid-like shape is indicative of either "active" or immature microglia. While we cannot rule out that mutant microglia were more activated, we propose microglia exhibited developmental delay similar to that observed in synaptic spine maturation in mice [21]. Indeed, a recent preprint [85] showed similar microglia neoteny in *SRGAP2C* mouse and human cell models. To connect our findings in zebrafish to humans, we detected high and conserved expression of *SRGAP2*, as well as *SRGAP2C*, in microglia derived from human adult post-mortem brain tissue. Remarkably, transcriptomic changes of microglia derived from *SRGAP2C* humanized zebrafish larvae versus controls resemble those from humans versus nonhuman primates. Most overlapping DEGs function in actin-cytoskeleton dynamics (down) and cell-cell interactions (up). This provides molecular evidence of altered membrane dynamics of human microglia compared with other primates, consistent

with the reduced ramifications observed for adult human microglia compared with macaque and marmoset imaged from post-mortem brain samples [54].

The most striking results produced by our transcriptomic analysis implicates vision development in *SRGAP2* mutants, a function never-before reported in genetic models of *SRGAP2*. Crystallins were amongst the highest upregulated genes found at 5 dpf (Figure 2B). While these genes are typically associated with lens development, we observed no gross morphological defects in the lenses of stable homozygous knockout larvae or adults (data not included). Delving into possible cellular drivers of the vision signatures identified in bulk data, we found *srgap2* to be highly expressed in axonal-rich regions of the zebrafish eyes (ON and retinal GCL), in line with *Srgap2* expression observed in mouse GCL [86]. Interestingly, upregulation of crystallin genes has also been reported in the retinas of *Srgap2*$^{+/-}$ adult mice [27]. Apha-crystallins, which encode heat-shock proteins, have been associated with axonal elongation [87] and regeneration [88]. Examining altered genes in *SRGAP2* zebrafish mutant retinal cells pointed to increased expression of axogenesis genes, also observed in human retinal organoids when compared to a nonhuman primate (rhesus macaque). Given that axonal guidance is critical for establishing vision [89], we tested whether *SRGAP2*-alterations in the retinas could impact visual processing in developing larvae. Assays testing the visual-motor responses of zebrafish larvae to abrupt light-dark changes or moving contrast stimuli [72,90] consistently showed that *srgap2* knockout and *SRGAP2C*-expressing larvae have an increased response to visual cues, suggestive of higher visual information processing capabilities.

Given the presence of *srgap2*-expressing microglia in the developing zebrafish eye, we propose a model where predominantly-amoeboid mutant microglia plays a role in retinal axon extension. Microglia are resident macrophages in the brain that migrate into the central nervous system early in development influencing wide-ranging developmental processes such as synaptogenesis and pruning, neurogenesis, and axogenesis [91,92]. The eye is among the first regions to be colonized by microglia, at ~26–30 hpf in zebrafish [57], with preferential localization to differentiating cells in the retina GCL [59] (also evident in our Tg[*mpeg1.1*:GFP] lines at 3 dpf, Figure 4B). *SRGAP2*-mutant microglia, in their immature and potentially activated state, could play a role in increased clearance of dead/apoptotic cells or pruning axons/synapses leading to altered retinal connectivity and improved visual processing. Further, beyond impacts in the eye, it is plausible that microglia mediate other brain phenotypes observed in *SRGAP2* mutant zebrafish. This has recently been proposed for changes in synaptic development of cortical pyramidal neurons observed in a microglia-specific *Srgap2* conditional knockout mouse model [85]. While we have yet to directly connect *SRGAP2*-related microglia functions to the observed changes in Exc:Inh neuronal balance of our mutant zebrafish, studies have found that microglial activation induces increased frequency of excitatory synaptic events [93]. Microglia are also associated with pro- and anti-epileptic activity due to their various roles in brain homeostasis and neuroinflammation [94] suggesting possible connections with seizures detected in our *SRGAP2* mutants. Moving forward, generation of microglia-specific *SRGAP2* zebrafish models will allow us to delineate microglia functions in retina and brain development.

While our studies using zebrafish have allowed us to query novel *SRGAP2* functions at an organismal level, they also present some limitations. “Humanizing” larvae by injection of *SRGAP2C* mRNA at the single-cell stage introduces the gene ubiquitously. While this could result in off-target phenotypes, all published studies to date suggest SRGAP2C functions solely by antagonizing *srgap2* making functions in non-relevant cells/tissues unlikely. A strength of this approach is that SRGAP2C-driven antagonism

potentially produces more severe phenotypes as it avoids the genetic compensation that can occur in knockout models [83]. This might explain differences in fold-change of DEGs between *srgap2* knockout and humanized models (Figure 2B), in particular across vision-related genes (Note S1). Nevertheless, to avoid possible confounding factors, our conservative transcriptome analysis considered only DEGs observed in both knockout and humanized *SRGAP2* models. Further, because SRGAP2C was transiently introduced, we only characterized phenotypes in zebrafish larvae up to 7 dpf, limiting the scope of our study to early developmental traits. Finally, the structure of the zebrafish forebrain, which lacks a neocortex, limits analysis of certain processes specific to mammals, such as subtle circuit changes between cortical regions observed in *SRGAP2* mouse models [22]. Regardless, conservation at cellular and molecular levels has successfully enabled zebrafish models of neurodevelopmental conditions impacting the cortex, such as autism and intellectual disability, across hundreds of genes [95–100]

In summary, we have leveraged the advantages of viable *SRGAP2* zebrafish models to investigate its functional roles. Our findings are concordant with previous reports implicating *SRGAP2* in neurological phenotypes and reveal novel functions in microglia and the developing eye. Combined, these results provide new hypotheses regarding *SRGAP2C*-driven changes to microglia function and axogenesis in the brain and retina unique to humans, as well as improvements in visual perception, that will be exciting to test in cross-species comparisons moving forward.

Methods

Zebrafish lines and husbandry

NHGRI-1 wild type zebrafish lines [101] were maintained using standard protocols [102], with animals maintained in a controlled temperature (28±0.5°C) and light (10 h dark/14 h light cycle) system with UV-sterilized filtered water (Aquaneering, San Diego, CA). Feeding and general assessments of health were performed twice a day, with feeding including rotifers (Rotigrow Nanno, Reed Mariculture, Campbell, CA), brine shrimp (Artemia Brine Shrimp 90% hatch, Aquaneering, San Diego, CA), and flakes (Zebrafish Select Diet, Aquaneering, San Diego, CA). For all assays, randomly selected pairs of adults were placed in 1 liter crossing tanks (Aquaneering, San Diego, CA) in a 1 male:1 female ratio, combining embryos from at least five simultaneous crosses. Embryos were then kept in standard Petri dishes with E3 media (0.03% Instant Ocean salt in deionized water) and grown in an incubator at 28±0.5°C, monitoring their health with a dissecting microscope (Leica, Buffalo Grove, IL). Transgenic lines used for this project were obtained via respective material transfer agreements and included: Tg[*vglut2a*:DsRed] [50] from Dr. Hitoshi Okamoto at the RIKEN Brain Science Institute in Japan, Tg[*dlx6a*:GFP] [49], and Tg[mpeg1.1:GFP] [58] from the Zebrafish International Resource Center. Zebrafish were staged as previously described [32]. All animal use was approved by the Institutional Animal Care and Use Committee from the Office of Animal Welfare Assurance, University of California, Davis.

Protein conservation assessment

Coding sequences for the largest transcript for human *SRGAP2* (ENSG00000266028), *SRGAP2C* (ENSG00000171943), mouse *Srgap2* (ENSMUSG00000026425), zebrafish *srgap2*

(ENSDARG00000032161), human *SRGAP3* (ENSG00000196220), mouse *Srgap3* (ENSMUSG00000030257), zebrafish *srgap3* (ENSDARG00000060309), human *SRGAP1* (ENSG00000196935), mouse *Srgap1* (ENSMUSG00000020121), zebrafish *srgap1a* (ENSDARG00000007461), and zebrafish *srgap1b* (ENSDARG00000045789) were downloaded from ENSEMBL [103]. Sequence alignments were performed using the R package *msa* and genetic distances estimated with *seqinr*. Phylogenetic trees were created using the Unweighted Pair Group Method with Arithmetic Mean (UPGMA) with the *hclust* function from the *stats* package. Protein domains were extracted using the UniProtKB/Swiss-Prot database[104] and conservation estimated with the protein BLAST tool [105]. Lastly, we used the *Dscript* tool[29] to predict protein-protein interactions between FBAR domains in human, mouse, and zebrafish SRGAP2 orthologs.

Protein co-immunoprecipitation

HEK 293T cells were co-transfected with plasmids encoding zebrafish Srgap2-HA and human SRGAP2C-GFP, or zebrafish Srgap2-HA and GFP alone, using the TurboFect™ transfection reagent (Thermo Scientific, R0533) according to manufacturer's instruction. 24 h after transfection, cells were lysed in 500 µl of Lysis Buffer (20 mM Tris-HCl, pH 8.0, 100 mM KCl, 5 mM $MgCl_2$, 0.2 mM EDTA, 10% glycerol, and 0.1% Tween 20) containing 1x protease inhibitor cocktails (Sigma-Aldrich, P8340). The lysates were gently rocked back and forth for 10 min at 4°C and then cleared by centrifugation at 14,000x g for 5 min at 4°C. 50 µl of the supernatant was saved as the input and the remaining 450 µl was subjected to immunoprecipitation. To capture GFP and GFP fusion proteins, 30 µl of GFP-nanobody conjugated agarose beads—a gift of Henry Ho and prepared as described in [106]—was washed and blocked with 1 ml of 0.01% bovine serum albumin (BSA) in phosphate-buffered saline (PBS) for 1 h at 4°C before mixed with the supernatant. The supernatant-beads mix was rocked back and forth for 1 h at 4°C. The beads were then washed with 1 ml of Lysis Buffer three times, 5 min each. The bound proteins were eluted by incubating the beads in 25 µl of 4x Laemmli sample buffer (125 mM Tris-HCl, pH 6.8, 4% sodium dodecyl sulfate, 40% glycerol, 10% 2-mercaptoethanol, and 0.01% Bromophenol blue) at 95°C for 10 min. Proteins in the eluates were then resolved by 10% sodium dodecyl sulfate polyacrylamide gel electrophoresis (SDS-PAGE) and transferred to a polyvinylidene difluoride (PVDF) membrane. After transfer, the PVDF membrane was cut horizontally between 125- and 90-kDa protein markers and blocked in Intercept™ Blocking Buffer (LI-COR, 927-60001) for 1 h at RT. The top half was then incubated with the anti-HA antibody (1:10,000 dilution, Invitrogen, 26183) and the bottom half was incubated with the anti-GFP antibody (1:10,000 dilution, Proteintech, 66002-1-lg) in Intercept™ Blocking Buffer for 1 h at RT. After the primary antibody incubation, membranes were washed with Tris-buffered saline (20 mM Tris-HCl, pH 7.6, and 150 mM NaCl) containing 0.1% Tween 20 (TBS-T) three times, 5 min each, and incubated with the IRDye 800RD anti-mouse IgG secondary antibody (1:30,000 dilution, LI-COR, 926-68070) in Intercept™ Blocking Buffer for 1.5 h at RT. Membranes were then washed with TBS-T three times, 5 min each, dried, and imaged using the Odyssey DLx imaging system (LI-COR, Model 9142).

Baseline expression of *srgap2*

We analyzed public RNA-seq data[30] that included five biological replicates of pools of 12 embryos at 18 different developmental timepoints to extract the expression of *srgap2* throughout development.

Additionally, RNA-seq from embryonic and adult tissues was retrieved from a recent study[33]. Raw reads were processed using *fastqc* [107], *trimmomatic*[108], and *salmon* [109] to obtain the transcripts per kilobase million (TPM) values. Validation of *srgap2* temporal expression during development was performed by quantitative PCR (qPCR) at selected timepoints. For this, five NHGRI-1 zebrafish pairs were crossed at each timepoint and three pools of embryos (20 embryos each) collected for whole RNA extraction using the RNeasy kit (Qiagen, Hilden, Germany) with gDNA eliminator columns for DNA removal. The qPCR reactions were prepared following the standard protocol for the Luna kit (New England Biolabs, Ipswich, MA). Sequences for all oligonucleotides used are in Table S2.

RNA *in situ* hybridization

Whole embryo *in situ* hybridizations were performed as previously described [110]. Total RNA was extracted from zebrafish wild type embryos using Trizol and the riboprobe generated from a pBS-SK-*srgap2* plasmid using a 20 µl *in vitro* transcription reaction containing ~300 ng of purified plasmid, 2 µl of 10x reaction buffer (New England Biolabs, Ipswich, MA), 2 µl DTT 0.1 M, 2 µl of 10x DIG labeling mix 10x DIG labeling mix (Roche, Basel, Switzerland), 0.5 µl of RiboLock RNase inhibitor (Thermo Fisher, Waltham, MA), 0.5 µl of RNA polymerase (T7 or T3), and completed with nuclease-free water. Reactions were incubated at 37°C for 2 h, followed by the addition of 1 µl TURBO DNase (Thermo Fisher, Waltham, MA) and 30 min incubation at 37°C. After this, reactions were stopped by adding 2 µl of STOP buffer (Promega, Madison, WI). Riboprobe purification was performed with precipitation in 2 µl of 5 M LiCl and 90 µl of 100% ethanol overnight at -80°C. Wild type PTU-treated 24 and 72 hpf embryos were manually dechorionated, fixed in 4% paraformaldehyde in 1x PBS overnight at 4°C, and treated with 10 µg/ml Proteinase K at room temperature for 10 min. Hybridization media included 65% formamide, 5x SSC, 0.1% Tween 20, 50 µg/ml heparin, 500 µg/ml Type X tRNA, and 9.2 mM citric acid. Embryos were pre-hybridized for 3 h in a 68°C water bath, followed by hybridization with 200 ng of riboprobe in an overnight 68°C water bath. After this, embryos were successively washed at 70°C with hybridization media, 2x SSC, and 0.2x SSC. Following this, embryos were finally washed with 1x PBS containing 0.1% Tween-20 (1x PBS-Tw) at room temperature. Then, embryos were incubated for 4 h in blocking solution (2% sheep serum, 2 mg/ml BSA, 1x PBS-Tw) and incubated overnight with blocking solution and 1:5000 diluted anti-DIG antibody (Sigma Aldrich, St. Louis, MO) at 4°C. After incubation, embryos were washed with 1x PBS-Tw and AP buffer (100 mM Tris pH 0.5, 100 mM NaCl, 5 mM $MgCl_2$, 0.1% Tween-20) at room temperature right before staining with NBT and BCIP substrates (Roche, Basel, Switzerland) in AP Buffer. Images were obtained using glycerol and a stereomicroscope (M165, Leica, Wetzlar, Germany) with a Leica DFC7000 T digital camera.

Generation of *srgap2* knockout zebrafish

srgap2 was disrupted in wild type zebrafish using CRISPR/Cas9 similar to previously performed[111,112]. The Alt-R system from Integrated DNA Technologies (IDT, Newark, NJ) was used, with the following crRNA sequences: GGUCUUGCAGGAGCUGCACACGG (targeting exon 3), CGCUGAUCUGGGCGAAGCGUGGG (targeting exon 4), GAGAGAGUCAGGUGAGCGAGGGG (targeting exon 6), and GUCUCCUGCUAAAUUCCGAAAGG (targeting exon 2,). All gRNA sequences were designed using the CRISPRScan tool with the GRCz11/danRer11 genome reference[113] (sequences

found in Table S2). In brief, 2.5 µl of 100 µM crRNA, 2.5 µl of 100 µM tracrRNA (IDT, Newark, NJ), and 5 µl of Nuclease-free Duplex Buffer (IDT, Newark, NJ) were annealed in a program of 5 min at 95°C, a ramp from 95°C to 50°C with a -0.1°C/s change, 10 min at 50°C, and a ramp from 50°C to 4°C with a -1°C/s change. Injection mixes were prepared with 1.30 µl of SpCas9 (20 µM, New England BioLabs, Ipswich, MA), 1.60 µl of annealed crRNA:tracrRNA, 2.5 µl of 4x Injection Buffer (0.2% phenol red, 800 mM KCl, 4 mM $MgCl_2$, 4 mM TCEP, 120 mM HEPES, pH 7.0), and 4.6 µl of Nuclease-free water. If several crRNAs were prepared in the same injection mix, equimolar quantities of each crRNA:tracrRNA were included.

We microinjected one-cell stage zebrafish embryos as described previously[112]. Briefly, needles were obtained from a micropipette puller (Model P-97, Sutter Instruments) and injections were performed with an air injector (Pneumatic MPPI-2 Pressure Injector). Embryos were collected and ~1 nl of injection mix injected per embryo, after previous calibration with a microruler. We used two approaches to generate *srgap2* knockouts, one by injecting an injection mix including all 4 gRNAs coupled with SpCas9, and another with an injection mix of the gRNA targeting exon 4 coupled with SpCas9 to create a stable line carrying one specific nonsense mutation. To generate the stable *srgap2* knockout line, we outcrossed our G_0-injected fish to wild type NHGRI-1 at ~1.5 months post-fertilization to obtain the G_1 heterozygous generation, which was further screened by sequencing (EZ-Amplicon sequencing, Azenta, Burlington, MA) a ~200 bp region that included the gRNA target site (primer sequences in Table S2). Specific alleles were defined using R package *CrispRVariants*[114]. We focused on a 5-bp deletion in exon 4 referred to as $srgap2^{tup\Delta5}$.

CRISPR off-target evaluation

Assessment of potential off-target sites for the gRNAs used was performed by Sanger sequencing the top predicted off-target sites from previously generated CIRCLE-seq libraries for each gRNA[115], following the standard protocol[116,117], and the top ten off-target sites were predicted using CRISPRScan[113] (Table S3). Injections of each gRNA were performed as previously described for subsequent DNA extraction at 5 dpf of injected and non-injected batch-sibling controls and Sanger sequencing (Azenta, Burlington, MA).

Injection of human mRNA in zebrafish

Temporal expression of the mRNA from human-specific *SRGAP2C* in the zebrafish was performed similarly to previously described[118,119]. Mammalian expression vector pEF-DEST51 containing *SRGAP2C* was used to produce 5'-capped mRNA using the MEGAshortscript T7 transcription kit (Thermo Fisher, Waltham, MA) following the manufacturer's guidelines with a 3.5 h 56°C incubation with T7 polymerase. mRNA was then purified with the MEGAclear transcription clean-up kit (Thermo Fisher, Waltham, MA), measured using a Quibit (Thermo Fisher, Waltham, MA) and evaluated for integrity by 2% agarose gel electrophoresis. The injection mix contained 100 ng/µl of mRNA, 4x Injection Buffer (0.2% phenol red, 800 mM KCl, 4 mM $MgCl_2$, 4 mM TCEP, 120 mM HEPES, pH 7.0), and nuclease-free water. As described above, one-cell stage zebrafish embryos were injected with ~1 nl of the injection mix and kept at 28°C until needed for different assays.

Morphometric measurements

High-throughput imaging of the zebrafish larvae was performed using the VAST BioImager system (Union Biometrica, Holliston, MA) as previously described[40,115]. In brief, 5 dpf larvae were placed in a rotating 600 µm capillary that coupled with a camera allows for the automatic acquisition of images from all four sides. Images were automatically processed using FishInspector v1.7[41] to identify and extract different morphological shapes, which were then analyzed with the *TableCreator* tool. Images with general issues (e.g., dead or truncated larvae) were discarded. In total, we measured the central line, head area, euclidean distance between the eyes, and the head-trunk angle across 331 larvae. As no significant differences in measurements of any feature were observed between our controls (uninjected NHGRI-1 wild type larvae, wild type larvae from the stable *srgap2* knockout line, and wild type NHGRI-1 larvae injected with SpCas9 coupled with a scrambled gRNA; all pairwise t-tests p-values > 0.05, complete results in Table S26), we merged these larvae in one "control" group.

Bulk RNA-seq

Gene expression differences across groups were investigated using RNA-seq. For the stable *srgap2* knockout larvae, a minimum of 3 different *srgap2*$^{+}$/*srgap2*$^{tup\Delta 5}$ x *srgap2*$^{+}$/*srgap2*$^{tup\Delta 5}$ crosses were set and embryos pooled in the same batch and larvae kept at 28°C until 5 dpf when they were fast frozen and placed in RNA later (Thermo Fisher, Waltham, MA). Tails were then cut off each larva for genotyping via high resolution melt (HRM) curve in a CFX 96 Real-Time System qPCR machine (BioRad). HRM mix included 5 µl DreamTaq DNA polymerase (Thermo Fisher, Waltham, MA), 0.5 µl of each primer at 10 µM, 1 µl of 1x SYBR green (Thermo Fisher, Waltham, MA) and 2 µl of nuclease-free water. Additionally, in parallel, wild type crosses were set and one-cell stage embryos injected with human *SRGAP2C* mRNA or the G_0-knockouts (injected with SpCas9 coupled with the 4 guide RNAs). Injections were performed as previously described, using ~1 nl of the injection mix. For all samples, the heads of five larvae were pooled together and RNA extracted using the RNeasy kit (Qiagen, Hilden, Germany) with gDNA eliminator columns for DNA removal. In total, three samples per group were harvested. Total RNA was then submitted for RNA-seq using poly-A selection and standard library preparation for Illumina sequencing (Genewiz, South Plainfield, NJ).

In a similar manner, 3'-tagged RNA-seq was performed for gene expression evaluations in earlier timepoints. For this, *srgap2* knockouts (stable and pooled), *SRGAP2C*-mRNA injected, and controls were co-injected with SpCas9 and a scrambled gRNA were obtained as previously described. Embryos from each group were collected at 24 (n= 20 per sample), 48 (n= 10 per sample), and 72 hpf (n= 10 per sample) for fast-freezing and incubation in RNAlater (Thermo Fisher, Waltham, MA) at -20C, completing three replicates per group per timepoint. Once all samples were collected, heads were dissected from all embryos and RNA extracted using the RNeasy kit (Qiagen, Hilden, Germany). RNA samples were submitted to the UC Davis DNA Technologies Core (Davis, CA) for library preparation and sequencing.

All raw RNA-seq reads were trimmed using *trim-galore* and then mapped to the published zebrafish optimized transcriptome[120] using *STAR*[121]. Gene-level counts were obtained with *HTseq*[122]. Overall,

samples exhibited high correlations in gene counts for both the RNA-seq (mean Spearman ρ= 0.97, range 0.95-0.99) and 3'-tagged RNA-seq (mean Spearman ρ= 0.88, range 0.85-0.93). Differentially expressed genes obtained with *DESeq2*[123] using the wild type samples from the stable line as controls for the stable knockouts and injection controls (SpCas9 coupled with a scrambled gRNA) for the G_0-knockouts and *SRGAP2C*-injected embryos. All enrichment tests of gene groups in specific biological pathways were performed using *clusterProfiler* [124] with the background genes including all expressed genes in the dataset.

Single-cell RNA-seq

Cellular composition differences across *SRGAP2* zebrafish lines were assessed using scRNA-seq. For this, *srgap2* knockouts (*srgap2*$^{tup\Delta5}$/*srgap2*$^{tup\Delta5}$ and G_0), *SRGAP2C*-injected, and SpCas-scrambled gRNA coupled-injected embryos were generated as previously described and incubated at 28°C. At 3 dpf, the heads of larvae from each group were dissected after euthanasia in cold tricaine (0.025%), pooling 30 heads together per sample (n= three samples per group) and immediately proceeding with cell dissociation. Dissociation was performed using previous protocols as reference [125,126], with two washes in 1 ml cold 1x PBS on ice and immediate incubation at 28°C for 15 min in a preheated dissociation mix that included 480 µl of 0.25% trypsin-EDTA (Thermo Fisher, Waltham, MA) and 20 µl of collagenase P (100 mg/ml, Sigma-Aldrich, St. Louis, MO). Every 5 min all samples were gently pipetted using a cut-open P1000 tip to increase complete dissociation. After 15 min, 800 µl stop solution (DMEM with 10% FBS) was added to each sample and immediately centrifuged at 700 g in 4°C for 5 min. The supernatant was discarded and cells were resuspended in cold 1x PBS for another 5 min centrifugation at 700 g in 4°C. After this, the supernatant was discarded and cells were resuspended in 800 ul suspension solution (DMEM with 10% FBS) and filtered through a Flowmi 40 µm cell strainer (Sigma Aldrich, St. Louis, MO) into a low-bind DNA tube (Eppendorf, Hamburg, Germany). All samples were then counted using a Countess II (Thermo Fisher, Waltham, MA) and cell viability was confirmed to be >65%. Cell fixation and library preparation were then performed with the Parse Biosciences Fixation and Single Cell Whole Transcriptome kit v1.3.0 (Parse Biosciences, Seattle, WA), following the manufacturer's instructions. A total of 12,500 cells per well were loaded into the barcoding plate and two resulting sub-libraries were sequenced in a NovaSeq 6000 platform.

Raw FASTQ scRNA-seq reads were processed using the Parse Biosciences processing pipeline v0.9.3 and the optimized zebrafish transcriptome[120] to obtain the gene x cell matrix files per sample. These matrices were processed into Seurat objects using *Seurat* v4[127] and quality control filtering included feature counts above 200 and below two standard deviations from the mean (5727 features), less than 5% mitochondrial or ribosomal percentages, and doublets removal with *DoubletFinder* [128] with a 4% expected doublets for the SPLiT-seq method[129]. Data for an average of 2391±250 cells per sample were obtained (full sample information in Table S9), which were normalized using *SCTransform* with the top 5,000 variable genes and regressing for mitochondrial and ribosomal percentages. Samples were then integrated using a canonical correlation analysis reduction[127] and nearest-neighbor graphs constructed using the first 15 principal components with the *FindNeighbors* function. Hierarchical clustering was performed with the euclidean distance between principal components embeddings (tree cut at k=40) and cluster marker genes obtained with *PrepSCTFindMarkers* and *FindAllMarkers* using the wilcox test option (parameters: *logfc.threshold*= 0.1, *min.pct*= 0.1, *return.thresh*= 0.01, *only.pos*= TRUE), which

were further detailed using zebrafish brain atlases[45,46] and the ZFIN database [130]. For the pseudo-bulk analysis, count data was aggregated using *AggregateExpression* and the differential expression test between cell types of different genotypes (e.g., mutant microglia cells vs control microglia cells) performed with the MAST test option[131] (parameters: *logfc.threshold*= 0.02, *min.pct*= 0.1, *only.pos*= FALSE). Several functions from *scCustomize*[132] were used for making plots.

Knockout models exhibited significantly reduced *srgap2* expression (ANOVA genotype effect *p*-value= 3.15×10^{-4}, Hom *p*-value= 5.80×10^{-4}, G_0-knockouts *p*-value= 0.011, Table S9), while no reduction was observed in the *SRGAP2C*-injected samples (*SRGAP2C*-humanized *p*-value= 0.992, Table S9), consistent with observations from our quantitative RT-PCR results (Figure S1A). Bulk RNA-seq showed high correlation with single-cell pseudo-bulk gene counts of the same genotype at 3 dpf (average Spearman ρ across genotypes= 0.76±0.03, all *p*-values < 2.2×10^{-16}).

Quantification of neuronal populations

srgap2 G_0-knockouts, *SRGAP2C*-mRNA injected, and SpCas9-scrambled-gRNA injected controls were created as previously described in embryos from a Tg[*vglut2*:DsRed] x Tg[*d1x6a*:GFP] cross. Embryos were kept at 28°C until 3 dpf, when larvae were anesthetized in tricaine (0.0125%) and embedded in 1% low-melting agarose (n= 6–7 per group). These embryos were imaged using a spinning disk confocal microscope system (Dragonfly, Andor Technology, Belfast, United Kingdom) housed inside an incubator (Okolab, Pozzouli, Italy) with Leica 10x and 20x objectives and an iXon camera (Andor Technology, Belfast, United Kingdom). All imaging was performed using Z-stacking of 10 µm slices starting in the dorsal-most part going ventrally until no fish was detected. Image processing was done using Fiji[133] by generating hyperstacks with maximum intensity projections and quantifying all areas either GFP or DsRed positive.

Motion-tracking activity screen

We performed motion-tracking recordings of 4 dpf *srgap2* knockout ($srgap2^{tupΔ5}/srgap2^{tupΔ5}$ and G_0), *SRGAP2C*-mRNA injected, and SpCas9-scrambled gRNA-injected larvae using the Zebrabox system with a camera acquisition speed of 30 frames per second (ViewPoint, Montreal, Canada). Larvae were placed in a 96-well plate with 150 µl of E3 media with 0 mM or 2.5 mM pentylenetetrazol (PTZ, #P6500, Sigma-Aldrich, St. Louis, MO) and their movement was recorded for 15 min. Then, a published MATLAB script was used to extract high-speed movement (>28 mm/s) events from data extracted in 1 s bins[53] and compared across groups.

Electrophysiology

Larvae (n= 20–30) from G_0 knockouts, *SRGAP2C*-mRNA injected, and SpCas9-scrambled gRNA-injected controls at 4 dpf were randomly selected for local field potential (LPF) recordings, as previously described[53]. Briefly, larvae were exposed to pancuronium (300 µM) and immobilized in 2% low-melting agarose in a vertical slice perfusion chamber (Siskiyou Corporation, #PC-V, Grant Pass, OR). These chambers were then placed on an upright microscope (Olympus BX-51W, Lausanne, Switzerland) and

monitored with a Zeiss Axiocam digital camera. 15 min LFP recordings were obtained by placing a single-glass microelectrode (WPI glass #TW150 F-3) with a ~1 µm tip diameter in the optic tectum under visual guidance. The voltage signals were filtered at 1 kHz and digitized at 10 kHz using Digidata 1320 A/D interface (Molecular Devices, San Jose, CA). All recordings were coded and scored independently by three researchers using Clampfit software (Molecular Devices, San Jose, CA) to obtain the final LFP score per group.

Histology and Immunostaining

We evaluated the general morphology of the eye in 5 dpf larvae from *srgap2*$^{tup\Delta5}$/*srgap2*$^{tup\Delta5}$, *SRGAP2C*-mRNA injected, and SpCas9-scrambled gRNA injected controls and performed immunohistochemistry using anti-Pax6 antibodies (Thermo Fisher, Waltham, MA) to label the amacrine and retinal ganglion cells in the eyes. In brief, 10 µm sections for each group were collected using a cryostat microtome (Leica, Wetzlar, Germany) and placed on slides at -80°C. Slides were then brought to room temperature and washed with 1 ml 1x PBS for 5 min, followed by incubation with blocking buffer (4% milk/TST buffer) for 1 h. Then, the blocking buffer was removed, and slides were incubated with the anti-Pax6 antibodies in blocking buffer overnight at 4°C. Secondary antibody anti-mouse (Thermo Fisher, Waltham, MA) was performed for 1 h after a wash with fresh blocking buffer. Images were obtained using a confocal microscope (Olympus, Lausanne, Switzerland). Additionally, cryosections (10 µm) from each group were stained for histology via hematoxylin and eosin (H&E) and mounted in Permount.

Visual-motor response assays

We performed visual-motor response tests on 5 dpf *srgap2*$^{tup\Delta5}$/*srgap2*$^{tup\Delta5}$, *SRGAP2C*-mRNA injected, pooled knockouts, and SpCas9-scrambled gRNA-injected larvae, in a 96-well plate with 150 µl E3 media per well (n= 24 per group). Using the Zebrabox system (ViewPoint, Montreal, Canada), we exposed larvae to a protocol consisting of 10 min dark adaptation followed by bright light (100 lumens) and recorded their movement responses. Movement data were exported in 1 s bins for comparisons across groups in the 20 s prior and post dark-to-light change. Additionally, we performed optomotor response (OMR) tests following a protocol that uses a monitor to display a video with 30 s periods of contrasting stripes moving at 1.04 rad/s separated by 20s intervals[71]. We placed 4 larvae per group in a standard Petri dish and exposed them to 5 cycles of the recording, with 3 replicates per group (n= 12 larval measurements per group). In separate experiments, video recordings were paused during every cycle, after exactly 10 s (halfway through the video) and the number of larvae with rostral ends oriented in the direction of the moving stripes were counted, giving the "OMR positive" response. The quantification was performed blinded from genotype.

Microglia morphology and abundance

One-cell stage larvae from a Tg[*mpeg1.1*:GFP] cross were microinjected similar as described above to generate *srgap2* G_0-knockouts, *SRGAP2C*-injected, and scrambled gRNA-injected controls. At 3 and 7 dpf larvae were anesthetized with MS-222 (0.175 mg/ml in E3 media), embedded in 1% low-melt agar, and immediately imaged in a spinning disk confocal microscope system (Dragonfly, Andor Technology,

Belfast, United Kingdom) as described before, using a 63x magnification lens to image individual cells. Sphericity was obtained as described before[60,134] using the Imaris software (Bitplane, Switzerland) and creating 3D surface reconstructions per cell. Parameters were consistent across samples, including a smooth selection of 0.191µm and thresholding of absolute intensity. A total of one to five microglial cells were imaged from three to four larvae per genotype at each timepoint. In addition, abundance of microglial cells in *SRGAP2* mutants (*srgap2* G_0-knockouts and *SRGAP2C*-injected) and scrambled gRNA-injected controls was assessed following an established protocol[57,135] by incubating 3 dpf larvae in E3 media containing 2.5 µg/ml neutral red at 28.5°C for 3 hr, followed by two water changes and imaged immediately after in an stereoscope (M165, Leica, Wetzlar, Germany) with a Leica DFC7000 T digital camera.

Human and non-human primates scRNA-seq

scRNA-seq data from human retinal organoids [66] (43,857 cells), human donors [68] (183,808 cells), macaque retinal organoids [67] (19,894 cells), macaque donors [68] (165,681 cells), and prefrontal cortex data from humans and non-human primates[64] (171,997 human cells, 158,099 chimpanzee cells, 131,032 macaque cells, 149,468 marmoset cells) were downloaded as preprocessed objects. Retinal datasets were integrated using the LIGER method for cross-species analyses [136] followed by joint matrix factorization with *optimizeALS* using a lambda of 5, a convergence threshold of $1x10^{-10}$, and a k of 30. Differentially expressed genes were obtained with *getFactorMarkers*, using the human data as reference. Enrichment of genes in biological pathways was performed using *clusterProfiler* [124]. For the prefrontal cortex data [64], we obtained differentially expressed genes with the *FindMarkers* function from Seurat v4.0 [127] using the wilcox test option. Microglial cells defined in the prefrontal cortex[64] and the middle temporal gyrus [137] were gathered totaling 30,918 cells (prefrontal cortex: human= 7,556, chimpanzee= 5,748, macaque= 8,058, marmoset= 4,626; middle temporal gyrus: human= 1,263, chimpanzee= 252, macaque= 942, marmoset= 2473) and their expression aggregated using *AggregateExpression* from Seurat [127] grouping by organism to obtain a gene by organism pseudocount table. Differential gene expression between species was then performed with *DESeq2* [123] and overrepresentation tests in GO terms with DAVID [138].

Statistical analysis

All statistical analyses were performed in R version 4.0.2, and all scripts are available in the github repository https://github.com/mydennislab/public_data/ (zenodo pending). Comparisons between groups were performed using two-tailed Student's T-tests, Mann-Whitney U-tests, Analysis of Variance (ANOVA) or nonparametric Dunn's tests, depending on the normality of the data assessed using the Shapiro-Wilk test. All analyses comparing across different experimental batches included *batch* as a factor in the model to control for biases caused by inter-batch differences. Fisher's exact tests were used for testing significant overlaps between gene lists. All mean values reported include their standard deviation unless otherwise noted. Significance thresholds were defined with an alpha of 0.05 and the proper corrections for multiple comparisons defined in the text. All gene ontology enrichment tests were performed using solely the expressed genes as the background gene list.

Data availability

GEO numbers of our deposited data pending: bulk RNA-seq, scRNA-seq

Figure Legends

Figure 1. Functional analysis of *srgap2* in the developing zebrafish. (A) Phylogenetic tree of the human, mice, and zebrafish SRGAP proteins based on their whole-protein amino acid identity using the Unweighted Pair Group Method with Arithmetic Mean method. Schematic of *SRGAP2* gene family evolutionary history across human chromosome 1 [25]. Previous studies have shown that SRGAP2 functions after homodimerization in concert with F-actin (brown oval) to dictate cell membrane dynamics, among other functions, and can also heterodimerize with SRGAP2C producing no functional product. (**B)** Co-immunoprecipitation of human-specific SRGAP2C and zebrafish Srgap2 in HEK293T cells showed interaction between these proteins. (**C)** Temporal expression of *srgap2* in the developing embryo, plotted using public RNA-seq data [30] (black line represents the best fit line with the standard error in dark gray) and normalized quantitative RT-PCR data from whole-embryo RNA collected at 6, 10, 24, 72, and 120 hpf (blue boxes, each dot represents a biological replicate). The light-gray box represents a critical neurogenesis stage in zebrafish development between 6 and 24 hpf [31]. (**D)** *srgap2* expression in different embryonic (24 hpf) and adult (>12 months old) tissues from a published RNA-seq dataset [33]. (**E)** Spatial expression of *srgap2* at 24 hpf and 3 dpf via *in situ* hybridization. Scale bar 100 µm. **(F)** Knockout *srgap2* zebrafish were created using two approaches, one in a stable knockout line by injecting SpCas9 coupled with one gRNA targeting exon 4, and another following a pooled approach co-injecting SpCas9 coupled with four gRNAs targeting early exons. Humanized larvae were created by injecting *in vitro* transcribed *SRGAP2C* mRNA at the one-cell stage.

Figure 2. Developmental and cellular phenotypes of diverse zebrafish models of *SRGAP2*. (**A)** Measurements of central line distance (ANOVA: $F_{(4, 321)}$= 12.84, genotype effects *p*-value= $1.04x10^{-9}$, FDR-adjusted *p*-values Het= $4.40x10^{-7}$, Hom= $6.29x10^{-7}$, Pooled= 0.015, *SRGAP2C*= $1.36x10^{-4}$), euclidean distance between the eyes (ANOVA: $F_{(4,321)}$= 23.49, genotype effects *p*-value= $4.72x10^{-17}$, Dunnett's test FDR-adjusted *p*-values: Het= $6.77x10^{-11}$, Hom= $4.69x10^{-10}$, Pooled= 0.05, *SRGAP2C*= $2.19x10^{-9}$), and head angle (ANOVA: $F_{(4,315)}$= 0.49, genotype effects *p*-value= 0.746) in 5 dpf larvae from stable *srgap2* knockout (Het n= 43, Hom n= 86), G_0 knockouts (n= 34), *SRGAP2C*-injected (n= 44), and control larvae (n= 124). Dots represent an imaged larva with the color indicating the imaging plate (a co-variable included in the statistical analyses). The red dotted line corresponds to the mean value for the control group. Representative images of each measurement are included on the top of each plot. (**B)** Correlation of the fold change (FC) between *srgap2* G_0-knockouts and *SRGAP2C*-injected larvae at 5 dpf, with common DEGs highlighted (red= upregulated (FC > 2), blue= downregulated (FC < -2)). Top representative GO terms enriched in common DEGs between *srgap2* G_0-knockouts and *SRGAP2C*-injected larvae (complete results in Table S5). Color of the bar represents the direction of the genes (red= commonly upregulated, blue= commonly downregulated). (**C)** Correlation of the FC between *srgap2* G_0-knockouts and *SRGAP2C*-injected larvae across development using data from 24, 48, and 72 hpf larvae, with common DEGs highlighted, complete results can be found in Tables S7, S8. (**D)** Clustering of the 28,687 profiled cells colored as 24 cell types based on the expression of gene markers. Expression of *srgap2* across cell types (left side, shaded in gray), with the size of the circle representing the percentage of cells in that cluster expressing *srgap2* and the color of the circle the average scaled expression in the

cluster. Enrichment test for the overlap between marker genes for each cell type and the differentially expressed genes at 3 dpf from bulk RNA-seq data (right side), with the size of the circle representing the odds ratio for the enrichment and the color of the circle the -log(BH-adjusted *p*-value) of the Fisher's exact test. Asterisks indicate an FDR-adjusted *p*-value < 0.05.

Figure 3. Neuronal alterations in *SRGAP2* mutants. (**A)** Neuronal clusters (hypothalamus, thalamus, optic tectum, hindbrain, purkinje cells, and neurons rich in glutamate receptors) selected to perform a differential gene expression test was performed to DEGs in the *SRGAP2* mutants compared to the control group. Barplot represents the top GO terms overrepresented in the 14 commonly upregulated genes (complete results in Table S14). (**B)** Ratio of cells classified as excitatory (*vglut2*$^{+}$) to inhibitory (*gad1b*$^{+}$) between the *srgap2* G_0-knockouts, *SRGAP2C*-injected, and controls (*srgap2* G_0 knockouts: 0.78±0.15, *p*-value= 0.031; *SRGAP2C*-injected: 0.82±0.09, *p*-value= 0.017, controls= 0.57±0.13; t-tests versus controls). (**C)** Ratio of excitatory (*vglut2*:DsRed+) to inhibitory (*dlx6*:GFP) cell area quantified from images of 3 dpf *srgap2* G_0-knockout, *SRGAP2C*-injected, SpCas9 control injected, and uninjected wild type larvae (G_0 knockout: Exc:Inh ratio=1.21±0.07, *p*-value=3.0x10^{-4}, *SRGAP2C*: Exc:Inh ratio= 1.16±0.05, *p*-value= 7.0x10^{-4}, SpCas9-injected controls Exc:Inh ratio= 0.98±0.03, p-value= 0.959; Mann-Whitney U-tests *p*-values vs wild-type controls). Images include representative samples per group, scale bars 100 µm. (**D)** High-speed events (HSE, >28 mm/s) identified in 15 min recordings of 4 dpf larvae (*srgap2* knockouts (stable Hom_{parent} and G_0), *SRGAP2C*-injected, and SpCas9-injected controls, n= 36 larvae per group) with and without PTZ. Frequency of HSE per min were compared to controls (0 mM PTZ: ANOVA *p*-value for genotypic effect= 0.415, average HSE/min= 0.006±0.02, no significant differences between groups; 2.5 mM PTZ: ANOVA genotype effect *p*-value= 1.1x10-6, Hom_{parent}= 0.010, G_0-knockouts= 2.2x10^{-6}, *SRGAP2C*-injected= 3.90x10^{-5}). **(E)** Local field potential (LFP) recordings in the optic tectum of 4 dpf larvae (G_0-knockouts, *SRGAP2C*-injected, and SpCas9-injected controls, n=21-30 per group) were obtained and scored by two independent researchers. Representative traces per group are shown. Asterisks in graphs represent a *p*-value below 0.05 for the comparison against the control group. ns= not significant.

Figure 4. Cross-species conservation of *SRGAP2* as a microglial gene. (**A)** Top GO terms with significant overrepresentation in genes upregulated (red) or downregulated (blue) in microglial cells from *SRGAP2* mutants from Figure 2D. (**B)** Sphericity values for individual microglial cells (mpeg1.1^{+}) at 3 and 7 dpf in *srgap2* knockouts, *SRGAP2C*-injected, and scrambled gRNA-injected controls. Each dot represents a single microglial cell (average of 4-5 cells per larvae from 3-4 larvae per genotype per timepoint were obtained). Representative images for the median sphericity value of larvae at 3 and 7 dpf for each genotype are included below the graph (scale bars: top images= 100µm, bottom images= 5 µm) . Asterisks denote a Tukey *post*-hoc p-value < 0.05. 3dpf: *srgap2* G_0 knockouts: 0.70±0.09, *p*-value= 0.0085; *SRGAP2C*-injected: 0.73±0.09, *p*-value= 0.0021, controls: 0.58±0.12; 7dpf: *srgap2* G_0 knockouts: 0.74±0.11, *p*-value < 2.2x10^{-16}; *SRGAP2C*-injected: 0.78±0.08, *p*-value < 2.2x10^{-16}, controls: 0.46±0.13. (**C)** Evaluation of 610,596 prefrontal cortex cells from human, chimpanzee, macaque, and marmoset (human: 171,997, chimpanzee: 158,099, macaque: 131,032, marmoset: 149,468) showing the levels of *SRGAP2* and *SRGAP2C* expression across species, highlighting the microglial cluster with a dotted square. Micro: microglia. Expression of *SRGAP2* and *SRGAP2C* in microglial subtypes across species with subtypes ordered from highest expression left to right. huMicro: human-specific microglia, hoMicro: Hominidae-specific microglia. **(D)** Microglial cells from human, chimpanzee, macaque, and marmoset

(human: 8,819 cells, chimpanzee: 6,000 cells, macaque: 9,000 cells, marmoset: 7,099 cells) from the prefrontal cortex and middle temporal gyrus were used to identify common DEGs between human and non-human primates, finding 340 common upregulated and 323 common downregulated genes. Top GO terms with significant overrepresentation in common DEGs are included.

Figure 5. *SRGAP2* impacts the retina. (**A)** Section of a 3 dpf NHGRI-1 larva staining *srgap2* expression via *in situ* hybridization, labeling predominantly the optic nerve (ON), retinal pigmented epithelium (RPE), and the ganglion cell layer (GCL). D: dorsal, V: ventral. (**B)** Retinal ganglion cells (RGCs) were selected and a differential gene expression performed between *SRGAP2*-mutants (*srgap2* knockouts and *SRGAP2C*-injected) versus controls, identifying 60 upregulated genes and 84 downregulated genes, with their top overrepresented GO terms included in barplots. **(C)** Human and macaque cells from retinal organoids (43,857 human and 19,894 macaque) were integrated to identify genes with increased expression in either species, with their top overrepresented GO terms included in barplots (complete results in Tables S22 and S23). (**D)** Motion response to changes in light were assessed in 4 dpf *srgap2* knockouts (Hom_{parent} and G_0-knockouts), *SRGAP2C*-injected, and SpCas9-scrambled gRNA-coupled control larvae using a 10 min acclimation period followed by an abrupt light change. Plot includes trend lines for change in distance moved observed in each evaluated group (n= 24 per group, standard error for each line included as a shaded gray), which were different between all groups compared to controls (Kolmogorov-smirnov tests *p*-values: $Hom_{parent}= 9.16x10^{-11}$, G_0-knockouts= $5.93x10^{-8}$, *SRGAP2C*-injected= $1.11x10^{-12}$). (**E)** Optomotor responses were evaluated in 4 dpf larvae using an optimized protocol[71] that quantifies the percentage of larvae relative to moving stripes. Boxplot includes the percentage of OMR-positive larvae (aligned to the visual stimulus) in *srgap2* knockouts (Hom_{parent} and G_0-knockouts) and *SRGAP2C*-injected, which was higher compared to controls (Dunn's Benjamini-Hochberg adjusted *p*-values: $Hom_{parent}= 0.0113$, G_0-knockouts= 0.0040, *SRGAP2C*-injected= 0.0040). Asterisks denote a *p*-value below 0.05.

Acknowledgements

We thank Kyle Burbach, Daisy Castillo, Aarthi Sekar, Alexandra Colón-Rodríguez, and Eva Ferino for their support in helping to generate and maintain the *srgap2* stable knockout line. We also thank Colin Shew, Jennielee Mia, Xueer Jiang, and Ingrid Brust-Mascher for technical support in computational and imaging analyses. We thank Bruce Draper, Kristen Kwan, Heather Mefford, Anna La Torre, Ala Moshiri, Nick Marsh-Armstrong, and Paul FitzGerald for many fruitful discussions, ideas, reagents, and advice. We thank the Cell Biology and Human Anatomy Department at UC Davis School of Medicine for the support to use multiple imaging equipment. This work was supported, in part, by the U.S. National Institutes of Health (NIH) grants from the Office of the Director and National Institute of Mental Health (DP2MH119424 and R01MH132818 to M.Y.D.), UC Davis MIND Institute Intellectual and Developmental Disabilities Research Center pilot grant (U54 HD079125 to M.Y.D.), NIH National Institute of General Medical Sciences (R01GM144435 to L.-E.J.), NIH National Institute of Neurological Disorders and Stroke (R01NS096976 and R01NS103139 to S.C.B.), NIH National Institute of Neurological Disorders and Stroke (R01NS109176 to S.S.), and a UC Davis Graduate Research Award (J.M.U-S.).

References

1. Pääbo, S. (2014). The Human Condition—A Molecular Approach. Preprint, https://doi.org/10.1016/j.cell.2013.12.036 https://doi.org/10.1016/j.cell.2013.12.036.

2. Varki, A., and Altheide, T.K. (2005). Comparing the human and chimpanzee genomes: searching for needles in a haystack. Genome Res. *15*, 1746–1758.

3. Ohno, S. (1970). Evolution by Gene Duplication.

4. Zhang, J. (2003). Evolution by gene duplication: an update. Trends Ecol. Evol. *18*, 292–298.

5. Bailey, J.A., Yavor, A.M., Massa, H.F., Trask, B.J., and Eichler, E.E. (2001). Segmental duplications: organization and impact within the current human genome project assembly. Genome Res. *11*, 1005–1017.

6. Dennis, M.Y., Harshman, L., Nelson, B.J., Penn, O., Cantsilieris, S., Huddleston, J., Antonacci, F., Penewit, K., Denman, L., Raja, A., et al. (2017). The evolution and population diversity of human-specific segmental duplications. Nat Ecol Evol *1*, 69.

7. Bailey, J.A., Gu, Z., Clark, R.A., Reinert, K., Samonte, R.V., Schwartz, S., Adams, M.D., Myers, E.W., Li, P.W., and Eichler, E.E. (2002). Recent segmental duplications in the human genome. Science *297*, 1003–1007.

8. Conrad, B., and Antonarakis, S.E. (2007). Gene duplication: a drive for phenotypic diversity and cause of human disease. Annu. Rev. Genomics Hum. Genet. *8*, 17–35.

9. Sudmant, P.H., Huddleston, J., Catacchio, C.R., Malig, M., Hillier, L.W., Baker, C., Mohajeri, K., Kondova, I., Bontrop, R.E., Persengiev, S., et al. (2013). Evolution and diversity of copy number variation in the great ape lineage. Genome Res. *23*, 1373–1382.

10. Marques-Bonet, T., Kidd, J.M., Ventura, M., Graves, T.A., Cheng, Z., Hillier, L.W., Jiang, Z., Baker, C., Malfavon-Borja, R., Fulton, L.A., et al. (2009). A burst of segmental duplications in the genome of the African great ape ancestor. Nature *457*, 877–881.

11. Marques-Bonet, T., Girirajan, S., and Eichler, E.E. (2009). The origins and impact of primate segmental duplications. Trends Genet. *25*, 443–454.

12. Sudmant, P.H., Kitzman, J.O., Antonacci, F., Alkan, C., Malig, M., Tsalenko, A., Sampas, N., Bruhn, L., Shendure, J., 1000 Genomes Project, et al. (2010). Diversity of human copy number variation and multicopy genes. Science *330*, 641–646.

13. Soto, D.C., Uribe-Salazar, J.M., Shew, C.J., Sekar, A., McGinty, S.P., and Dennis, M.Y. (2023). Genomic structural variation: A complex but important driver of human evolution. Am J Biol Anthropol *181 Suppl 76*, 118–144.

14. Guerrier, S., Coutinho-Budd, J., Sassa, T., Gresset, A., Jordan, N.V., Chen, K., Jin, W.-L., Frost, A., and Polleux, F. (2009). The F-BAR domain of srGAP2 induces membrane protrusions required for neuronal migration and morphogenesis. Cell *138*, 990–1004.

15. Fiddes, I.T., Lodewijk, G.A., Mooring, M., Bosworth, C.M., Ewing, A.D., Mantalas, G.L., Novak, A.M., van den Bout, A., Bishara, A., Rosenkrantz, J.L., et al. (2018). Human-Specific NOTCH2NL

Genes Affect Notch Signaling and Cortical Neurogenesis. Cell *173*, 1356–1369.e22.

16. Florio, M., Albert, M., Taverna, E., Namba, T., Brandl, H., Lewitus, E., Haffner, C., Sykes, A., Wong, F.K., Peters, J., et al. (2015). Human-specific gene ARHGAP11B promotes basal progenitor amplification and neocortex expansion. Science *347*, 1465–1470.

17. Ju, X.-C., Hou, Q.-Q., Sheng, A.-L., Wu, K.-Y., Zhou, Y., Jin, Y., Wen, T., Yang, Z., Wang, X., and Luo, Z.-G. (2016). The hominoid-specific gene TBC1D3 promotes generation of basal neural progenitors and induces cortical folding in mice. Elife *5*. https://doi.org/10.7554/eLife.18197.

18. Fossati, M., Pizzarelli, R., Schmidt, E.R., Kupferman, J.V., Stroebel, D., Polleux, F., and Charrier, C. (2016). SRGAP2 and Its Human-Specific Paralog Co-Regulate the Development of Excitatory and Inhibitory Synapses. Neuron *91*, 356–369.

19. Libé-Philippot, B., Lejeune, A., Wierda, K., Vlaeminck, I., Beckers, S., Gaspariunaite, V., Bilheu, A., Nyitrai, H., Vennekens, K.M., Bird, T.W., et al. (2022). LRRC37B is a species-specific regulator of voltage-gated channels and excitability in human cortical neurons. bioRxiv, 2022.12.21.521423. https://doi.org/10.1101/2022.12.21.521423.

20. Van Heurck, R., Bonnefont, J., Wojno, M., Suzuki, I.K., Velez-Bravo, F.D., Erkol, E., Nguyen, D.T., Herpoel, A., Bilheu, A., Beckers, S., et al. (2023). CROCCP2 acts as a human-specific modifier of cilia dynamics and mTOR signaling to promote expansion of cortical progenitors. Neuron *111*, 65–80.e6.

21. Charrier, C., Joshi, K., Coutinho-Budd, J., Kim, J.-E., Lambert, N., de Marchena, J., Jin, W.-L., Vanderhaeghen, P., Ghosh, A., Sassa, T., et al. (2012). Inhibition of SRGAP2 function by its human-specific paralogs induces neoteny during spine maturation. Cell *149*, 923–935.

22. Schmidt, E.R.E., Zhao, H.T., Park, J.M., Dipoppa, M., Monsalve-Mercado, M.M., Dahan, J.B., Rodgers, C.C., Lejeune, A., Hillman, E.M.C., Miller, K.D., et al. (2021). A human-specific modifier of cortical connectivity and circuit function. Nature *599*, 640–644.

23. Dennis, M.Y., Nuttle, X., Sudmant, P.H., Antonacci, F., Graves, T.A., Nefedov, M., Rosenfeld, J.A., Sajjadian, S., Malig, M., Kotkiewicz, H., et al. (2012). Evolution of human-specific neural SRGAP2 genes by incomplete segmental duplication. Cell *149*, 912–922.

24. Schmidt, E.R.E., Kupferman, J.V., and Stackmann, M. (2019). The human-specific paralogs SRGAP2B and SRGAP2C differentially modulate SRGAP2A-dependent synaptic development. Scientific Reports *9*. https://doi.org/10.1101/596940.

25. Dennis, M.Y., and Eichler, E.E. (2016). Human adaptation and evolution by segmental duplication. Curr. Opin. Genet. Dev. *41*, 44–52.

26. Sporny, M., Guez-Haddad, J., Kreusch, A., Shakartzi, S., Neznansky, A., Cross, A., Isupov, M.N., Qualmann, B., Kessels, M.M., and Opatowsky, Y. (2017). Structural History of Human SRGAP2 Proteins. Mol. Biol. Evol. *34*, 1463–1478.

27. Gan, Y.-J., Cao, Y., Zhang, Z.-H., Zhang, J., Chen, G., Dong, L.-Q., Li, T., Shen, M.-X., Qu, J., and Chi, Z.-L. (2023). Srgap2 suppression ameliorates retinal ganglion cell degeneration in mice. Neural Regeneration Res. *18*, 2307.

28. Saitsu, H., Osaka, H., Sugiyama, S., Kurosawa, K., Mizuguchi, T., Nishiyama, K., Nishimura, A.,

Tsurusaki, Y., Doi, H., Miyake, N., et al. (2012). Early infantile epileptic encephalopathy associated with the disrupted gene encoding Slit-Robo Rho GTPase activating protein 2 (SRGAP2). Am. J. Med. Genet. A *158A*, 199–205.

29. Sledzieski, S., Singh, R., Cowen, L., and Berger, B. (2021). D-SCRIPT translates genome to phenome with sequence-based, structure-aware, genome-scale predictions of protein-protein interactions. Cell Syst *12*, 969–982.e6.

30. White, R.J., Collins, J.E., Sealy, I.M., Wali, N., Dooley, C.M., Digby, Z., Stemple, D.L., Murphy, D.N., Billis, K., Hourlier, T., et al. (2017). A high-resolution mRNA expression time course of embryonic development in zebrafish. Elife *6*. https://doi.org/10.7554/eLife.30860.

31. Schwarzer, S., Asokan, N., Bludau, O., Chae, J., Kuscha, V., Kaslin, J., and Hans, S. (2020). Neurogenesis in the inner ear: the zebrafish statoacoustic ganglion provides new neurons from a Neurod/Nestin-positive progenitor pool well into adulthood. Development *147*. https://doi.org/10.1242/dev.176750.

32. Kimmel, C.B., Ballard, W.W., Kimmel, S.R., Ullmann, B., and Schilling, T.F. (1995). Stages of embryonic development of the zebrafish. Dev. Dyn. *203*, 253–310.

33. Yang, H., Luan, Y., Liu, T., Lee, H.J., Fang, L., Wang, Y., Wang, X., Zhang, B., Jin, Q., Ang, K.C., et al. (2020). A map of cis-regulatory elements and 3D genome structures in zebrafish. Nature *588*, 337–343.

34. Varshney, G.K., Pei, W., LaFave, M.C., Idol, J., Xu, L., Gallardo, V., Carrington, B., Bishop, K., Jones, M., Li, M., et al. (2015). High-throughput gene targeting and phenotyping in zebrafish using CRISPR/Cas9. Genome Res. *25*, 1030–1042.

35. Varshney, G.K., Carrington, B., Pei, W., Bishop, K., Chen, Z., Fan, C., Xu, L., Jones, M., LaFave, M.C., Ledin, J., et al. (2016). A high-throughput functional genomics workflow based on CRISPR/Cas9-mediated targeted mutagenesis in zebrafish. Nat. Protoc. *11*, 2357–2375.

36. Thyme, S.B., Pieper, L.M., Li, E.H., Pandey, S., Wang, Y., Morris, N.S., Sha, C., Choi, J.W., Herrera, K.J., Soucy, E.R., et al. (2019). Phenotypic Landscape of Schizophrenia-Associated Genes Defines Candidates and Their Shared Functions. Cell *177*, 478–491.e20.

37. Shah, A.N., Davey, C.F., Whitebirch, A.C., Miller, A.C., and Moens, C.B. (2015). Rapid reverse genetic screening using CRISPR in zebrafish. Nat. Methods *12*, 535–540.

38. Kroll, F., Powell, G.T., Ghosh, M., Gestri, G., Antinucci, P., Hearn, T.J., Tunbak, H., Lim, S., Dennis, H.W., Fernandez, J.M., et al. (2021). A simple and effective F0 knockout method for rapid screening of behaviour and other complex phenotypes. Elife *10*. https://doi.org/10.7554/eLife.59683.

39. Wu, R.S., Lam, I.I., Clay, H., Duong, D.N., Deo, R.C., and Coughlin, S.R. (2018). A Rapid Method for Directed Gene Knockout for Screening in G0 Zebrafish. Dev. Cell *46*, 112–125.e4.

40. Pulak, R. (2016). Tools for automating the imaging of zebrafish larvae. Methods *96*, 118–126.

41. Teixidó, E., Kießling, T.R., Krupp, E., Quevedo, C., Muriana, A., and Scholz, S. (2019). Automated Morphological Feature Assessment for Zebrafish Embryo Developmental Toxicity Screens. Toxicol. Sci. *167*, 438–449.

42. Romo, L., Gold, N.B., and Walker, M.A. (2024). Endocrine features of primary mitochondrial

diseases. Curr. Opin. Endocrinol. Diabetes Obes. *31*, 34–42.

43. Marcó de la Cruz, B., Campos, J., Molinaro, A., Xie, X., Jin, G., Wei, Z., Acuna, C., and Sterky, F.H. (2024). Liprin-α proteins are master regulators of human presynapse assembly. Nat. Neurosci. *27*, 629–642.

44. Rosenberg, A.B., Roco, C.M., Muscat, R.A., Kuchina, A., Sample, P., Yao, Z., Graybuck, L.T., Peeler, D.J., Mukherjee, S., Chen, W., et al. (2018). Single-cell profiling of the developing mouse brain and spinal cord with split-pool barcoding. Science *360*, 176–182.

45. Raj, B., Farrell, J.A., Liu, J., El Kholtei, J., Carte, A.N., Navajas Acedo, J., Du, L.Y., McKenna, A., Relić, Đ., Leslie, J.M., et al. (2020). Emergence of Neuronal Diversity during Vertebrate Brain Development. Neuron *108*, 1058–1074.e6.

46. Zhang, H., Wang, H., Shen, X., Jia, X., Yu, S., Qiu, X., Wang, Y., Du, J., Yan, J., and He, J. (2021). The landscape of regulatory genes in brain-wide neuronal phenotypes of a vertebrate brain. Elife *10*. https://doi.org/10.7554/eLife.68224.

47. Cowan, C.A., Yokoyama, N., Bianchi, L.M., Henkemeyer, M., and Fritzsch, B. (2000). EphB2 guides axons at the midline and is necessary for normal vestibular function. Neuron *26*, 417–430.

48. Henkemeyer, M., Orioli, D., Henderson, J.T., Saxton, T.M., Roder, J., Pawson, T., and Klein, R. (1996). Nuk controls pathfinding of commissural axons in the mammalian central nervous system. Cell *86*, 35–46.

49. Yu, M., Xi, Y., Pollack, J., Debiais-Thibaud, M., Macdonald, R.B., and Ekker, M. (2011). Activity of dlx5a/dlx6a regulatory elements during zebrafish GABAergic neuron development. Int. J. Dev. Neurosci. *29*, 681–691.

50. Satou, C., Kimura, Y., and Higashijima, S.-I. (2012). Generation of multiple classes of V0 neurons in zebrafish spinal cord: progenitor heterogeneity and temporal control of neuronal diversity. J. Neurosci. *32*, 1771–1783.

51. Hoffman, E.J., Turner, K.J., Fernandez, J.M., Cifuentes, D., Ghosh, M., Ijaz, S., Jain, R.A., Kubo, F., Bill, B.R., Baier, H., et al. (2016). Estrogens Suppress a Behavioral Phenotype in Zebrafish Mutants of the Autism Risk Gene, CNTNAP2. Neuron *89*, 725–733.

52. Brenet, A., Hassan-Abdi, R., Somkhit, J., Yanicostas, C., and Soussi-Yanicostas, N. (2019). Defective excitatory/inhibitory synaptic balance and increased neuron apoptosis in a zebrafish model of Dravet syndrome. Preprint, https://doi.org/10.1101/781393 https://doi.org/10.1101/781393.

53. Griffin, A., Carpenter, C., Liu, J., Paterno, R., Grone, B., Hamling, K., Moog, M., Dinday, M.T., Figueroa, F., Anvar, M., et al. (2021). Phenotypic analysis of catastrophic childhood epilepsy genes. Commun Biol *4*, 680.

54. Geirsdottir, L., David, E., Keren-Shaul, H., Weiner, A., Bohlen, S.C., Neuber, J., Balic, A., Giladi, A., Sheban, F., Dutertre, C.-A., et al. (2019). Cross-Species Single-Cell Analysis Reveals Divergence of the Primate Microglia Program. Cell *179*, 1609–1622.e16.

55. Coutinho-Budd, J., Ghukasyan, V., Zylka, M.J., and Polleux, F. (2012). The F-BAR domains from srGAP1, srGAP2 and srGAP3 regulate membrane deformation differently. J. Cell Sci. *125*, 3390–3401.

56. Lucas, B., and Hardin, J. (2017). Mind the (sr)GAP - roles of Slit-Robo GAPs in neurons, brains and beyond. J. Cell Sci. *130*, 3965–3974.

57. Herbomel, P., Thisse, B., and Thisse, C. (2001). Zebrafish early macrophages colonize cephalic mesenchyme and developing brain, retina, and epidermis through a M-CSF receptor-dependent invasive process. Dev. Biol. *238*. https://doi.org/10.1006/dbio.2001.0393.

58. Ellett, F., Pase, L., Hayman, J.W., Andrianopoulos, A., and Lieschke, G.J. (2011). mpeg1 promoter transgenes direct macrophage-lineage expression in zebrafish. Blood *117*, e49–e56.

59. Ranawat, N., and Masai, I. (2021). Mechanisms underlying microglial colonization of developing neural retina in zebrafish. Elife *10*. https://doi.org/10.7554/eLife.70550.

60. Mazzolini, J., Le Clerc, S., Morisse, G., Coulonges, C., Kuil, L.E., van Ham, T.J., Zagury, J.-F., and Sieger, D. (2020). Gene expression profiling reveals a conserved microglia signature in larval zebrafish. Glia *68*, 298–315.

61. Woodburn, S.C., Bollinger, J.L., and Wohleb, E.S. (2021). The semantics of microglia activation: neuroinflammation, homeostasis, and stress. J. Neuroinflammation *18*, 1–16.

62. Stopper, L., Bălşeanu, T.A., Cătălin, B., Rogoveanu, O.C., Mogoantă, L., and Scheller, A. (2018). Microglia morphology in the physiological and diseased brain - from fixed tissue to in vivo conditions. Rom. J. Morphol. Embryol. *59*, 7–12.

63. Marsh, S.E., Walker, A.J., Kamath, T., Dissing-Olesen, L., Hammond, T.R., de Soysa, T.Y., Young, A.M.H., Murphy, S., Abdulraouf, A., Nadaf, N., et al. (2022). Dissection of artifactual and confounding glial signatures by single-cell sequencing of mouse and human brain. Nat. Neurosci. *25*, 306–316.

64. Ma, S., Skarica, M., Li, Q., Xu, C., Risgaard, R.D., Tebbenkamp, A.T.N., Mato-Blanco, X., Kovner, R., Krsnik, Ž., de Martin, X., et al. (2022). Molecular and cellular evolution of the primate dorsolateral prefrontal cortex. Science. https://doi.org/10.1126/science.abo7257.

65. Zhang, Y., and Beachy, P.A. (2023). Cellular and molecular mechanisms of Hedgehog signalling. Nat. Rev. Mol. Cell Biol. *24*, 668–687.

66. Cowan, C.S., Renner, M., De Gennaro, M., Gross-Scherf, B., Goldblum, D., Hou, Y., Munz, M., Rodrigues, T.M., Krol, J., Szikra, T., et al. (2020). Cell Types of the Human Retina and Its Organoids at Single-Cell Resolution. Cell *182*. https://doi.org/10.1016/j.cell.2020.08.013.

67. Jacobo Lopez, A., Kim, S., Qian, X., Rogers, J., Stout, J.T., Thomasy, S.M., La Torre, A., Chen, R., and Moshiri, A. (2022). Retinal organoids derived from rhesus macaque iPSCs undergo accelerated differentiation compared to human stem cells. Cell Prolif. *55*, e13198.

68. Hahn, J., Monavarfeshani, A., Qiao, M., Kao, A.H., Kölsch, Y., Kumar, A., Kunze, V.P., Rasys, A.M., Richardson, R., Wekselblatt, J.B., et al. (2023). Evolution of neuronal cell classes and types in the vertebrate retina. Nature *624*, 415–424.

69. Peng, Y.-R., Shekhar, K., Yan, W., Herrmann, D., Sappington, A., Bryman, G.S., van Zyl, T., Do, M.T.H., Regev, A., and Sanes, J.R. (2019). Molecular Classification and Comparative Taxonomics of Foveal and Peripheral Cells in Primate Retina. Cell *176*, 1222–1237.e22.

70. Lee, B.B., Martin, P.R., and Grünert, U. (2010). Retinal connectivity and primate vision. Prog.

Retin. Eye Res. *29*. https://doi.org/10.1016/j.preteyeres.2010.08.004.

71. LeFauve, M.K., Rowe, C.J., Crowley-Perry, M., Wiegand, J.L., Shapiro, A.G., and Connaughton, V.P. (2021). Using a variant of the optomotor response as a visual defect detection assay in zebrafish. J Biol Methods *8*, e144.

72. Emran, F., Rihel, J., Adolph, A.R., and Dowling, J.E. (2010). Zebrafish larvae lose vision at night. Proc. Natl. Acad. Sci. U. S. A. *107*, 6034–6039.

73. Emran, F., Rihel, J., and Dowling, J.E. (2008). A behavioral assay to measure responsiveness of zebrafish to changes in light intensities. J. Vis. Exp. https://doi.org/10.3791/923.

74. Kist, A.M., and Portugues, R. (2019). Optomotor Swimming in Larval Zebrafish Is Driven by Global Whole-Field Visual Motion and Local Light-Dark Transitions. Cell Rep. *29*, 659–670.e3.

75. Neuhauss, S.C., Biehlmaier, O., Seeliger, M.W., Das, T., Kohler, K., Harris, W.A., and Baier, H. (1999). Genetic disorders of vision revealed by a behavioral screen of 400 essential loci in zebrafish. J. Neurosci. *19*, 8603–8615.

76. Blockus, H., and Chédotal, A. (2016). Slit-Robo signaling. Development *143*, 3037–3044.

77. Ordan, E., and Volk, T. (2015). Cleaved Slit directs embryonic muscles. Fly *9*, 82–85.

78. Cheng, R.-K., Jesuthasan, S.J., and Penney, T.B. (2014). Zebrafish forebrain and temporal conditioning. Philos. Trans. R. Soc. Lond. B Biol. Sci. *369*. https://doi.org/10.1098/rstb.2012.0462.

79. Burgess, H.A., and Burton, E.A. (2023). A Critical Review of Zebrafish Neurological Disease Models−1. The Premise: Neuroanatomical, Cellular and Genetic Homology and Experimental Tractability. Oxford Open Neuroscience *2*. https://doi.org/10.1093/oons/kvac018.

80. Martin, A., Babbitt, A., Pickens, A.G., Pickett, B.E., Hill, J.T., and Suli, A. (2022). Single-Cell RNA Sequencing Characterizes the Molecular Heterogeneity of the Larval Zebrafish Optic Tectum. Front. Mol. Neurosci. *15*, 818007.

81. Akyuz, E., Polat, A.K., Eroglu, E., Kullu, I., Angelopoulou, E., and Paudel, Y.N. (2021). Revisiting the role of neurotransmitters in epilepsy: An updated review. Life Sci. *265*. https://doi.org/10.1016/j.lfs.2020.118826.

82. Niemeyer, J.E., Gadamsetty, P., Chun, C., Sylvester, S., Lucas, J.P., Ma, H., Schwartz, T.H., and Aksay, E.R.F. (2022). Seizures initiate in zones of relative hyperexcitation in a zebrafish epilepsy model. Brain *145*. https://doi.org/10.1093/brain/awac073.

83. El-Brolosy, M.A., Kontarakis, Z., Rossi, A., Kuenne, C., Günther, S., Fukuda, N., Kikhi, K., Boezio, G.L.M., Takacs, C.M., Lai, S.-L., et al. (2019). Genetic compensation triggered by mutant mRNA degradation. Nature *568*, 193–197.

84. Lesca, G., Rudolf, G., Bruneau, N., Lozovaya, N., Labalme, A., Boutry-Kryza, N., Salmi, M., Tsintsadze, T., Addis, L., Motte, J., et al. (2013). GRIN2A mutations in acquired epileptic aphasia and related childhood focal epilepsies and encephalopathies with speech and language dysfunction. Nat. Genet. *45*, 1061–1066.

85. Diaz-Salazar, C., Krzisch, M., Yoo, J., Nano, P.R., Bhaduri, A., Jaenisch, R., and Polleux, F. (2024). Human-specific paralogs of SRGAP2 induce neotenic features of microglia structural and functional

maturation. bioRxiv. https://doi.org/10.1101/2024.06.28.601266.

86. Bacon, C., Endris, V., and Rappold, G. (2009). Dynamic expression of the Slit-Robo GTPase activating protein genes during development of the murine nervous system. J. Comp. Neurol. *513*, 224–236.

87. Slingsby, C., and Wistow, G.J. (2014). Functions of crystallins in and out of lens: roles in elongated and post-mitotic cells. Prog. Biophys. Mol. Biol. *115*, 52–67.

88. Shao, W.-Y., Liu, X., Gu, X.-L., Ying, X., Wu, N., Xu, H.-W., and Wang, Y. (2016). Promotion of axon regeneration and inhibition of astrocyte activation by alpha A-crystallin on crushed optic nerve. Int. J. Ophthalmol. *9*, 955.

89. Burger, C.A., Jiang, D., Mackin, R.D., and Samuel, M.A. (2021). Development and maintenance of vision's first synapse. Dev. Biol. *476*. https://doi.org/10.1016/j.ydbio.2021.04.001.

90. Neuhauss, S.C.F. (2003). Behavioral genetic approaches to visual system development and function in zebrafish. J. Neurobiol. *54*, 148–160.

91. Thion, M.S., and Garel, S. (2017). On place and time: microglia in embryonic and perinatal brain development. Curr. Opin. Neurobiol. *47*, 121–130.

92. Li, Q., and Barres, B.A. (2017). Microglia and macrophages in brain homeostasis and disease. Nat. Rev. Immunol. *18*, 225–242.

93. Pascual, O., Ben Achour, S., Rostaing, P., Triller, A., and Bessis, A. (2012). Microglia activation triggers astrocyte-mediated modulation of excitatory neurotransmission. Proc. Natl. Acad. Sci. U. S. A. *109*, E197–E205.

94. Yu, C., Deng, X.-J., and Xu, D. (2023). Microglia in epilepsy. Neurobiol. Dis. *185*, 106249.

95. Veenstra-VanderWeele, J., O'Reilly, K.C., Dennis, M.Y., Uribe-Salazar, J.M., and Amaral, D.G. (2023). Translational Neuroscience Approaches to Understanding Autism. Am. J. Psychiatry *180*, 265–276.

96. Rea, V., and Van Raay, T.J. (2020). Using Zebrafish to Model Autism Spectrum Disorder: A Comparison of ASD Risk Genes Between Zebrafish and Their Mammalian Counterparts. Front. Mol. Neurosci. *13*, 575575.

97. Tayanloo-Beik, A., Hamidpour, S.K., Abedi, M., Shojaei, H., Tavirani, M.R., Namazi, N., Larijani, B., and Arjmand, B. (2022). Zebrafish Modeling of Autism Spectrum Disorders, Current Status and Future Prospective. Front. Psychiatry *13*, 911770.

98. Modeling autism spectrum disorders in zebrafish (2020). In Behavioral and Neural Genetics of Zebrafish (Academic Press), pp. 451–480.

99. Sakai, C., Ijaz, S., and Hoffman, E.J. (2018). Zebrafish Models of Neurodevelopmental Disorders: Past, Present, and Future. Front. Mol. Neurosci. *11*, 294.

100. Costa, F.V., Zabegalov, K.N., Kolesnikova, T.O., de Abreu, M.S., Kotova, M.M., Petersen, E.V., and Kalueff, A.V. (2023). Experimental models of human cortical malformations: from mammals to "acortical" zebrafish. Neurosci. Biobehav. Rev. *155*, 105429.

101. LaFave, M.C., Varshney, G.K., Vemulapalli, M., Mullikin, J.C., and Burgess, S.M. (2014). A defined zebrafish line for high-throughput genetics and genomics: NHGRI-1. Genetics *198*, 167–170.

102. Westerfield, M. (1995). The Zebrafish Book: A Guide for the Laboratory Use of Zebrafish (Danio Rerio).

103. Zerbino, D.R., Achuthan, P., Akanni, W., Ridwan Amode, M., Barrell, D., Bhai, J., Billis, K., Cummins, C., Gall, A., Girón, C.G., et al. (2018). Ensembl 2018. Preprint, https://doi.org/10.1093/nar/gkx1098 https://doi.org/10.1093/nar/gkx1098.

104. UniProt Consortium (2019). UniProt: a worldwide hub of protein knowledge. Nucleic Acids Res. *47*, D506–D515.

105. National Center for Biotechnology Information (Verenigde Staten). (2002). The NCBI Handbook.

106. Rothbauer, U., Zolghadr, K., Muyldermans, S., Schepers, A., Cardoso, M.C., and Leonhardt, H. (2008). A versatile nanotrap for biochemical and functional studies with fluorescent fusion proteins. Mol. Cell. Proteomics *7*, 282–289.

107. Andrews, S., and Others (2010). FastQC: a quality control tool for high throughput sequence data. Preprint at Babraham Bioinformatics, Babraham Institute, Cambridge, United Kingdom.

108. Bolger, A.M., Lohse, M., and Usadel, B. (2014). Trimmomatic: a flexible trimmer for Illumina sequence data. Bioinformatics *30*, 2114–2120.

109. Patro, R., Duggal, G., Love, M.I., Irizarry, R.A., and Kingsford, C. (2017). Salmon provides fast and bias-aware quantification of transcript expression. Nat. Methods *14*, 417–419.

110. Thisse, C., and Thisse, B. (2008). High-resolution in situ hybridization to whole-mount zebrafish embryos. Nat. Protoc. *3*, 59–69.

111. Jao, L.-E., Wente, S.R., and Chen, W. (2013). Efficient multiplex biallelic zebrafish genome editing using a CRISPR nuclease system. Proc. Natl. Acad. Sci. U. S. A. *110*, 13904–13909.

112. Jao, L.-E., Appel, B., and Wente, S.R. (2012). A zebrafish model of lethal congenital contracture syndrome 1 reveals Gle1 function in spinal neural precursor survival and motor axon arborization. Development *139*, 1316–1326.

113. Moreno-Mateos, M.A., Vejnar, C.E., Beaudoin, J.-D., Fernandez, J.P., Mis, E.K., Khokha, M.K., and Giraldez, A.J. (2015). CRISPRscan: designing highly efficient sgRNAs for CRISPR-Cas9 targeting in vivo. Nat. Methods *12*, 982–988.

114. Lindsay, H., Burger, A., Biyong, B., Felker, A., Hess, C., Zaugg, J., Chiavacci, E., Anders, C., Jinek, M., Mosimann, C., et al. (2016). CrispRVariants charts the mutation spectrum of genome engineering experiments. Nat. Biotechnol. *34*, 701–702.

115. Colón-Rodríguez, A., Uribe-Salazar, J.M., Weyenberg, K.B., Sriram, A., Quezada, A., Kaya, G., Jao, E., Radke, B., Lein, P.J., and Dennis, M.Y. (2020). Assessment of Autism Zebrafish Mutant Models Using a High-Throughput Larval Phenotyping Platform. Front Cell Dev Biol *8*, 586296.

116. Tsai, S.Q., Nguyen, N.T., Malagon-Lopez, J., Topkar, V.V., Aryee, M.J., and Joung, J.K. (2017). CIRCLE-seq: a highly sensitive in vitro screen for genome-wide CRISPR-Cas9 nuclease off-targets.

Nat. Methods *14*, 607–614.

117. Lazzarotto, C.R., Nguyen, N.T., Tang, X., Malagon-Lopez, J., Guo, J.A., Aryee, M.J., Joung, J.K., and Tsai, S.Q. (2018). Defining CRISPR-Cas9 genome-wide nuclease activities with CIRCLE-seq. Nat. Protoc. *13*, 2615–2642.

118. Shafik, A.M., and Cifuentes, D. (2018). Zebrafish as a Tool to Study Congenital Heart Diseases. Preprint, https://doi.org/10.1016/b978-0-12-809657-4.64146-7 https://doi.org/10.1016/b978-0-12-809657-4.64146-7.

119. Kretov, D.A., Shafik, A.M., and Cifuentes, D. (2018). Assessing miR-451 Activity and Its Role in Erythropoiesis. Methods Mol. Biol. *1680*, 179–190.

120. Lawson, N.D., Li, R., Shin, M., Grosse, A., Yukselen, O., Stone, O.A., Kucukural, A., and Zhu, L. (2020). An improved zebrafish transcriptome annotation for sensitive and comprehensive detection of cell type-specific genes. https://doi.org/10.7554/eLife.55792.

121. Dobin, A., Davis, C.A., Schlesinger, F., Drenkow, J., Zaleski, C., Jha, S., Batut, P., Chaisson, M., and Gingeras, T.R. (2013). STAR: ultrafast universal RNA-seq aligner. Preprint, https://doi.org/10.1093/bioinformatics/bts635 https://doi.org/10.1093/bioinformatics/bts635.

122. Putri, G.H., Anders, S., Pyl, P.T., Pimanda, J.E., and Zanini, F. (2022). Analysing high-throughput sequencing data in Python with HTSeq 2.0. Bioinformatics *38*, 2943–2945.

123. Love, M.I., Huber, W., and Anders, S. (2014). Moderated estimation of fold change and dispersion for RNA-seq data with DESeq2. Genome Biol. *15*, 550.

124. Yu, G., Wang, L.-G., Han, Y., and He, Q.-Y. (2012). clusterProfiler: an R package for comparing biological themes among gene clusters. OMICS *16*, 284–287.

125. Farnsworth, D.R., Saunders, L.M., and Miller, A.C. (2020). A single-cell transcriptome atlas for zebrafish development. Dev. Biol. *459*, 100–108.

126. Bresciani, E., Broadbridge, E., and Liu, P.P. (2018). An efficient dissociation protocol for generation of single cell suspension from zebrafish embryos and larvae. MethodsX *5*, 1287–1290.

127. Hao, Y., Hao, S., Andersen-Nissen, E., Mauck, W.M., 3rd, Zheng, S., Butler, A., Lee, M.J., Wilk, A.J., Darby, C., Zager, M., et al. (2021). Integrated analysis of multimodal single-cell data. Cell *184*, 3573–3587.e29.

128. McGinnis, C.S., Murrow, L.M., and Gartner, Z.J. (2019). DoubletFinder: Doublet Detection in Single-Cell RNA Sequencing Data Using Artificial Nearest Neighbors. Cell systems *8*, 329.

129. Tran, V., Papalexi, E., Schroeder, S., Kim, G., Sapre, A., Pangallo, J., Sova, A., Matulich, P., Kenyon, L., Sayar, Z., et al. (2022). High sensitivity single cell RNA sequencing with split pool barcoding. bioRxiv, 2022.08.27.505512. https://doi.org/10.1101/2022.08.27.505512.

130. Bradford, Y.M., Van Slyke, C.E., Ruzicka, L., Singer, A., Eagle, A., Fashena, D., Howe, D.G., Frazer, K., Martin, R., Paddock, H., et al. (2022). Zebrafish information network, the knowledgebase for Danio rerio research. Genetics *220*. https://doi.org/10.1093/genetics/iyac016.

131. Finak, G., McDavid, A., Yajima, M., Deng, J., Gersuk, V., Shalek, A.K., Slichter, C.K., Miller, H.W., Juliana McElrath, M., Prlic, M., et al. (2015). MAST: a flexible statistical framework for

assessing transcriptional changes and characterizing heterogeneity in single-cell RNA sequencing data. Genome Biol. *16*. https://doi.org/10.1186/s13059-015-0844-5.

132. Marsh, S.E., Salmon, M., and Hoffman, P. scCustomize: custom visualizations & functions for streamlined analyses of single cell sequencing. Preprint at https://doi. org/10.5281/zenodo.

133. Schindelin, J., Arganda-Carreras, I., Frise, E., Kaynig, V., Longair, M., Pietzsch, T., Preibisch, S., Rueden, C., Saalfeld, S., Schmid, B., et al. (2012). Fiji: an open-source platform for biological-image analysis. Nat. Methods *9*, 676–682.

134. Silva, N.J., Dorman, L.C., Vainchtein, I.D., Horneck, N.C., and Molofsky, A.V. (2021). In situ and transcriptomic identification of microglia in synapse-rich regions of the developing zebrafish brain. Nat. Commun. *12*, 5916.

135. Shiau, C.E., Monk, K.R., Joo, W., and Talbot, W.S. (2013). An anti-inflammatory NOD-like receptor is required for microglia development. Cell Rep. *5*, 1342–1352.

136. Welch, J.D., Kozareva, V., Ferreira, A., Vanderburg, C., Martin, C., and Macosko, E.Z. (2019). Single-Cell Multi-omic Integration Compares and Contrasts Features of Brain Cell Identity. Cell *177*, 1873–1887.e17.

137. Jorstad, N.L., Song, J.H.T., Exposito-Alonso, D., Suresh, H., Castro-Pacheco, N., Krienen, F.M., Yanny, A.M., Close, J., Gelfand, E., Long, B., et al. (2023). Comparative transcriptomics reveals human-specific cortical features. Science. https://doi.org/10.1126/science.ade9516.

138. Sherman, B.T., Hao, M., Qiu, J., Jiao, X., Baseler, M.W., Lane, H.C., Imamichi, T., and Chang, W. (2022). DAVID: a web server for functional enrichment analysis and functional annotation of gene lists (2021 update). Nucleic Acids Res. *50*. https://doi.org/10.1093/nar/gkac194.